metrology

MDPI

Review

Ultra-High-Pressure and Extreme-Pressure Metrology: A Review of Measurement Technologies and Traceability

Qiang Tong [1,*], Zihao Ma [1], Yang Wang [1], Yichao Li [1], Guibing Pang [1] and Yuanchao Yang [2,*]

[1] School of Mechanical Engineering and Automation, Dalian Polytechnic University, Dalian 116034, China; 240410802000393@xy.dlpu.edu.cn (Z.M.); 250440855000452@xy.dlpu.edu.cn (Y.W.); liyichao@dlpu.edu.cn (Y.L.); panggb@dlpu.edu.cn (G.P.)
[2] National Institute of Metrology, Beijing 100029, China
* Correspondence: tongqiang@dlpu.edu.cn (Q.T.); yangyc@nim.ac.cn (Y.Y.)

Abstract

Ultra-high-pressure and extreme-pressure metrology plays a critical role in advanced manufacturing, geoscience, high-pressure physics, and frontier materials research. As pressure ranges extend from hundreds of MPa to several GPa and beyond, pressure generation and measurement are increasingly constrained by material strength, structural deformation, the state of pressure-transmitting media, sealing reliability, sensor drift, and incomplete traceability chains, imposing higher requirements on pressure metrology. This review systematically examines measurement technologies and traceability routes for ultra-high-pressure and extreme-pressure ranges. The development of controlled-clearance piston gauges is summarized, with emphasis on uncertainty reduction, range extension, and calibration automation. Drop-weight-based primary standards for dynamic pressure are also reviewed as an established route for the traceable calibration of high-amplitude, millisecond-scale hydraulic pressure pulses. Progress in secondary ultra-high-pressure standards is reviewed, including ultra-high-pressure gauges and piezoresistive, resonant, fiber-optic, and triboelectric sensors, with focus on range extension, high-accuracy measurement, environmental adaptability, and emerging pressure-sensitive mechanisms. Measurement methods for extreme pressure, including ruby fluorescence, Raman spectroscopy, X-ray diffraction, phase-transition points, and equations of state, are compared in terms of applicability and limitations. Current challenges in ultra-high-pressure and extreme-pressure metrology are further discussed, together with the prospects of quantum pressure sensing based on nitrogen-vacancy centers in nanodiamonds, providing a reference for future research and metrological infrastructure development.

Keywords: ultra-high-pressure metrology; extreme pressure; pressure traceability; controlled-clearance piston gauge; pressure sensor; diamond anvil cell; quantum pressure sensing; measurement uncertainty

Check for updates

Academic Editors: Piotr Kuwalek, Grzegorz Wiczyński and Mariusz Rząsa

Received: 1 June 2026
Revised: 13 August 2026
Accepted: 22 August 2026
Published: 25 August 2026

Copyright: © 2026 by the authors. Licensee MDPI, Basel, Switzerland. This article is an open access article distributed under the terms and conditions of the Creative Commons Attribution (CC BY) license.

1. Introduction

Pressure is one of the most important physical quantities in industrial production, precision manufacturing, energy development, geoscience, and frontier materials research, where its accurate measurement and reliable traceability are directly related to process control, equipment safety, experimental reproducibility, and the comparability of scientific data [1–5]. As high-pressure technologies continue to extend toward higher pressure ranges, pressure metrology is no longer limited to instrument indications in industrial

measurement but has gradually evolved into an integrated metrological system involving pressure generation, pressure realization, standard transfer, sensor calibration, pressure-scale consistency, and uncertainty evaluation. In engineering applications, pressures above 100 MPa are commonly referred to as ultra-high pressures; at pressures above several GPa (1 GPa = 1000 MPa), the mechanical response of materials, pressure-generation methods, states of pressure-transmitting media, and pressure-measurement approaches all change substantially [6–10]. Therefore, for the purposes of this review, pressures from hundreds of MPa to several GPa are classified as ultra-high pressures, whereas pressures above several GPa are referred to as extreme pressure.

Ultra-high-pressure and extreme-pressure conditions are widely encountered in a variety of scientific and engineering scenarios, including high-pressure water jets, high-pressure food processing, and geoscience research, as shown in Figure 1 [11–27]. When pressures further increase beyond several GPa, factors such as material strength, structural deformation, the state of pressure-transmitting media, sealing performance, phase-transition behavior, and the stability of pressure scales can significantly affect pressure generation and measurement results [8,9,28,29]. In particular, under extreme-pressure conditions, conventional mechanical pressure standards are limited by material strength, piston–cylinder deformation, effective-area correction, and pressure-transmitting media, making it difficult for them to directly cover the full pressure range above several GPa [30]. Therefore, obtaining accurate, stable, comparable, and traceable pressure values under ultra-high-pressure and extreme-pressure conditions has become a key challenge shared by pressure metrology and extreme-condition science.

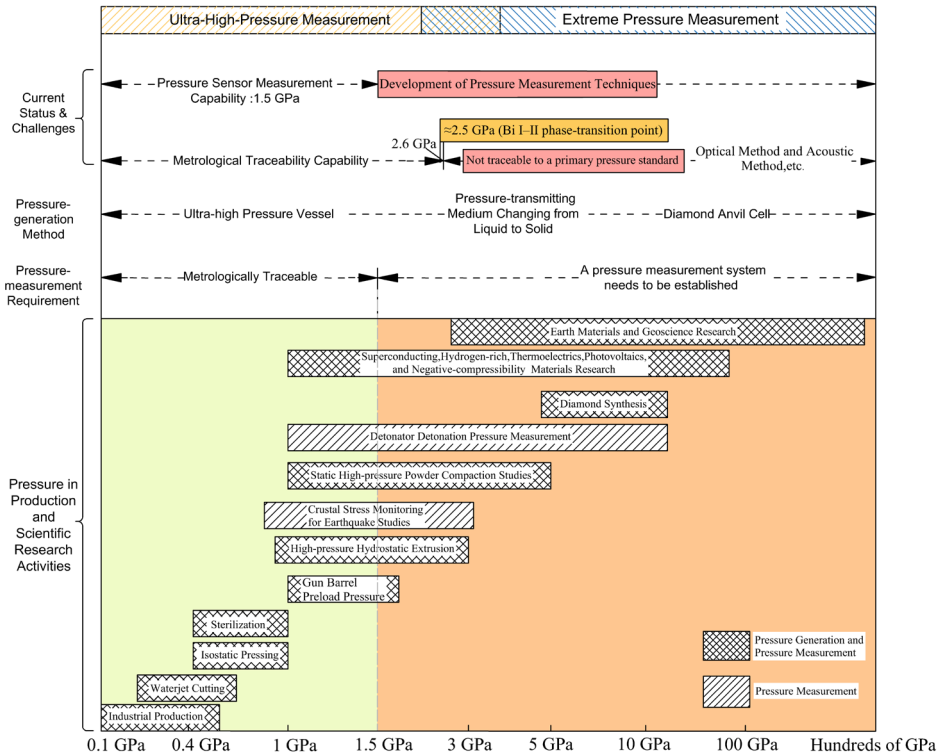


Figure 1. Representative applications and measurement methods across different pressure ranges. The pressure axis is schematic and not drawn to scale.

From the perspective of the metrological system, primary ultra-high-pressure standards mainly rely on controlled-clearance piston gauges (CCPGs) for pressure realization, together with devices such as pressure multipliers for pressure dissemination to higher pressure ranges [31]. A CCPG establishes the link between pressure and the International

System of Units (SI) through the applied mass load, local gravitational acceleration, effective area of the piston–cylinder assembly (PCA), and relevant correction terms, making it a core instrument for ultra-high-pressure calibration and pressure dissemination [32,33]. However, as pressure increases, factors such as elastic distortion of the PCA, pressure-dependent correction of the effective area, jacket-pressure control, the high-pressure viscosity of the pressure-transmitting medium, and the reliability of sealing structures significantly affect the measurement uncertainty of CCPGs and limit the extension of primary ultra-high-pressure standards toward higher pressure ranges [32,34–36]. As secondary measurement instruments, ultra-high-pressure gauges and pressure sensors can meet the requirements of pressure measurement in most scenarios after calibration against primary standards; however, their metrological reliability is still affected by calibration conditions, long-term drift, hysteresis, temperature sensitivity, packaging stress, and adaptability to extreme environments [37–42]. For dynamic pressure metrology, drop-weight-based primary standards have also been developed to generate traceable high-amplitude transient pressure pulses for the calibration of dynamic pressure transducers [43].

Extreme-pressure metrology usually relies on devices such as diamond anvil cells (DACs) to establish high-pressure experimental environments, with pressure measured using methods such as ruby fluorescence, Raman spectroscopy, X-ray diffraction, phase-transition points, and equations of state [44–47]. These methods have greatly extended the accessible pressure-measurement range, but most of them rely on reference materials or empirical or semi-empirical calibration relationships and still have incomplete traceability chains to the SI unit of pressure; therefore, the evaluation of their associated uncertainties and the consistency among different methods remain challenging [48]. Pressure-induced phase-transition points of materials such as bismuth in the low-GPa range can serve as discrete reference points for establishing a metrological link with primary pressure standards under certain conditions, but such reference points are inherently discrete and cannot by themselves form a continuous pressure traceability system covering the range from ultra-high pressure to extreme pressure [49–51]. Therefore, establishing metrological links between extreme-pressure measurement results and mechanical primary pressure standards, coordinating pressure-scale consistency among multiple pressure-measurement methods, and improving the pressure traceability chain covering ultra-high-pressure to extreme-pressure ranges are central issues in the development of current pressure metrology systems.

Existing reviews have provided comprehensive summaries of the historical development of pressure metrology, the classification of pressure-measurement methods, and the impact of SI revisions on pressure metrology, offering important references for understanding pressure metrology systems [52]. These reviews primarily focus on pressure metrology systems from atmospheric pressure to several GPa, while DAC-based methods for extreme-pressure metrology are discussed to a lesser extent. In addition, considerable progress has been made in recent years in CCPGs, ultra-high-pressure sensors, and various DAC-based extreme-pressure measurement methods. However, much of this work has been developed around individual instruments, specific measurement methods, or particular pressure ranges, leaving room for a more integrated discussion of the relationships among pressure realization, pressure dissemination, pressure-scale connection, and uncertainty evaluation across the ultra-high-pressure to extreme-pressure range. Therefore, a systematic review of recent technological advances in ultra-high-pressure and extreme-pressure metrology above 100 MPa is warranted.

This review focuses on ultra-high-pressure and extreme-pressure metrology technologies and their traceability systems. First, the current development of primary pressure standards, including CCPGs and pressure multipliers, is summarized, with emphasis on

key technologies such as effective-area determination, structural deformation correction, sealing systems, and pressure-transmitting media. Second, recent advances in ultra-high-pressure gauges and pressure sensors are reviewed in terms of digitalization, sensing materials, structural design, and adaptability to extreme environments. Subsequently, extreme-pressure measurement methods, including ruby fluorescence, Raman spectroscopy, X-ray diffraction, phase-transition points, and equations of state, are compared with respect to their applicability and traceability limitations. Finally, in light of emerging trends in quantum pressure sensing and frequency traceability, the opportunities and challenges associated with constructing a unified pressure metrology system covering the ultra-high-pressure to extreme-pressure range are discussed. This review provides a reference for improving pressure traceability systems across the range from ultra-high pressure above 100 MPa to extreme pressure.

2. Pressure Ranges, Measurement Principles, and Traceability Framework

2.1. Pressure Ranges of Ultra-High Pressure and Extreme Pressure

At present, there is no fully unified classification standard for pressure ranges across different disciplines and application scenarios. In engineering applications, when pressure reaches or exceeds 100 MPa, the stresses borne by conventional pressure vessels, hydraulic components, pipe fittings, and sealing structures increase substantially, and factors such as elastic deformation of materials, the contact state of sealing surfaces, changes in the viscosity of pressure-transmitting media, and the risk of system leakage become non-negligible [7,53–56]. Therefore, pressures above 100 MPa are commonly defined as ultra-high pressures in industrial practice, and this review likewise adopts 100 MPa as the starting point for discussing ultra-high pressure [57].

In the range from 100 MPa to several GPa, pressure is measured using instruments such as piston gauges and ultra-high-pressure sensors, and the pressure values remain traceable to the SI to some extent; however, these instruments are already constrained by multiple factors. Under high-pressure conditions, the PCA undergoes non-negligible elastic deformation, causing the effective area to vary with pressure rather than being treated simply as a constant; meanwhile, the viscosity of the pressure-transmitting medium increases significantly at high pressure, affecting the sensitivity of the pressure gauge; in addition, sealing structures must maintain reliable sealing performance under high pressure to prevent leakage [31,58–60].

When pressure exceeds several GPa and extends to higher ranges, both the pressure environment and the measurement mechanisms undergo more pronounced changes [61]. At this stage, the PCA structure faces more severe issues related to stress concentration, deformation, and effective-area stability, and its design often approaches the limits imposed by material strength and structural stability [62]. The viscosity of some commonly used pressure-transmitting media increases sharply above several GPa, and these media may even undergo vitrification or solidification, leading to reduced hydrostaticity and the formation of pressure gradients [63–66]. Therefore, mechanical pressure standards are difficult to extend directly to higher pressure ranges. In pressure environments above several GPa, materials may exhibit high-pressure physical responses, such as pressure-induced phase transitions, lattice compression, electronic-structure reconstruction, and abrupt changes in mechanical properties [67–70]. Under these conditions, conventional pressure-measurement methods become ineffective, and pressure calibration or indirect measurement must rely on methods such as ruby fluorescence, Raman spectroscopy, X-ray diffraction, phase-transition points, and equations of state. Based on these differences, and for the convenience of the following discussion, this review classifies the range from

100 MPa to several GPa as ultra-high pressure and the pressure range above several GPa as extreme pressure.

2.2. Ultra-High-Pressure and Extreme-Pressure Metrology Systems and Traceability Chains

From the perspective of the metrology system, pressure metrology can be divided into primary pressure standards and secondary pressure standards [71–73]. Primary pressure standards are directly traceable to the base units of the SI, and piston gauges can directly trace pressure to the SI over a wide measurement range [71,74]. Secondary pressure standards usually determine pressure by calibrating pressure-dependent changes in physical quantities, as in various sensors and optical pressure-measurement methods [75]. Within pressure ranges that can be directly calibrated, the value-realization capability and uncertainty level of primary pressure standards provide the basis for secondary-instrument calibration, pressure dissemination, and the comparability of measurement results.

For static and quasi-static ultra-high-pressure metrology systems, primary pressure standards are usually realized using CCPGs, which generate pressure values based on the applied mass load, local gravitational acceleration, the effective area of the PCA, and relevant correction terms. Owing to limitations related to material strength, sealing structures, and the performance of pressure-transmitting media, the highest measurement range of CCPGs reported in the open literature is currently 2.6 GPa [76]. The value of 2.6 GPa represents the highest reported operating pressure of a controlled-clearance dead-weight piston gauge in the cited historical literature. However, whether this value can be regarded as the upper limit of current SI-traceable ultra-high-pressure capability requires confirmation through an instrument-specific traceability chain, pressure-realization model, and comprehensive uncertainty evaluation. For dynamic ultra-high-pressure metrology, drop-weight-based primary standards generate short-duration, high-amplitude pressure pulses in a hydraulic medium through mechanical impact and provide a traceable route for calibrating dynamic pressure transducers over a demonstrated range of approximately 10–400 MPa [43]. Secondary pressure standards are mainly realized using ultra-high-pressure gauges and ultra-high-pressure sensors. These instruments do not usually realize pressure values directly but are instead calibrated against CCPGs to establish traceability to the SI. Among currently available secondary measurement instruments, the HP-2 pressure sensor developed by WIKA has a measurement range of up to 1500 MPa and a maximum measurement error of 0.5% FS.

For extreme-pressure metrology systems, conventional piston gauges are limited by material strength, structural deformation, sealing, and pressure-transmitting media, making it difficult for them to directly cover pressure ranges above several GPa. Therefore, direct traceability of extreme-pressure values to the SI remains highly challenging. Secondary pressure standards include optical and acoustic methods [77,78]. Among them, optical methods are widely used because of their relatively high stability. These methods calibrate pressure based on spectral changes under different pressure conditions and are suitable for pressure measurement in transparent chambers such as DACs [79]. However, the secondary values obtained using these methods are currently difficult to trace to primary standards, and uncertainty evaluation remains challenging.

The traceability chain for ultra-high-pressure metrology systems is relatively well established within their demonstrated operating ranges. Pressure sensors can be calibrated against CCPGs, which realize pressure from SI-traceable quantities including mass, local gravitational acceleration, and effective piston-cylinder area, together with the relevant deformation, temperature, and jacket-pressure corrections. This provides a documented route from primary pressure realization to calibrated gauges and sensors, with an uncertainty budget that can be evaluated for the complete measurement chain. Accordingly, the main

development directions in this range include extending the operating range of CCPGs, improving their stability and uncertainty, and enhancing the pressure capacity, long-term stability, and calibration performance of ultra-high-pressure sensors.

In contrast, the traceability framework for extreme-pressure measurement remains incomplete for two closely related reasons. Although diamond anvil cells (DACs) can generate very high pressures, the pressure at the sample position generally cannot be realized directly from the applied force and a known effective area, as in a piston gauge. Instead, it is usually inferred from pressure scales or pressure-dependent material responses, including ruby fluorescence, electrical resistivity, X-ray diffraction (XRD), Raman spectroscopy, equation-of-state (EOS) methods, and Mossbauer spectroscopy. This difference is not merely an extension of the measurement range but a change in the pressure-realization mechanism. In a CCPG, pressure is realized through a direct force-to-area relationship, whereas in a DAC, it is inferred from pressure-dependent material responses through a calibration scale or an equation-of-state model. Consequently, the SI-linked force-to-area relation established by the CCPG cannot be transferred continuously to the local sample position in the DAC without an intermediate scale-linkage procedure. The change in realization mechanism therefore introduces a discontinuity in the pressure traceability pathway and requires additional reference materials, calibration functions, and model-based corrections.

Discrete material phase transitions can provide calibration anchors for particular DAC pressure scales; for example, the Bi I-II transition has been used to calibrate the low-pressure R1-line shift of the ruby gauge [80]. The Bi I–II equilibrium pressure was reported as (2520 ± 5) MPa at 25 °C [81]. This value provides a quantitative reference at a single low-GPa pressure point but does not by itself validate the calibration function or EOS used to assign pressures between, or far beyond, discrete reference points. The uncertainty associated with the Bi I-II transition should be propagated to downstream DAC pressure scales using the relevant measurement model and the law of propagation of uncertainty specified in the Guide to the Expression of Uncertainty in Measurement (GUM), including the contributions and correlations of calibration-function parameters, reference-material responses, and any EOS parameters involved [82]. At 100 GPa and ambient temperature, the pressure derived from the Holmes Pt scale was reported to be at least 7% higher than that derived from some commonly used Au scales, while several newer ruby scales predicted pressures at least 4% higher than the widely used Mao ruby scale [83]. Fei et al. further reported pressure variations of up to 7% in the room-temperature megabar range for scales based on reduced shock-wave EOSs alone [83]. These reported differences demonstrate that discrete reference points alone are insufficient to establish a continuous and mutually consistent pressure-scale linkage across the extreme-pressure range. In practice, pressure determination between discrete reference points relies on pressure-scale calibration functions and reference materials and may involve EOS-based interpolation or extrapolation [83].

For extreme-pressure measurement, pressure transfer in DACs is governed by the hydrostaticity of the pressure-transmitting medium. The hydrostatic condition of a liquid pressure medium can be lost when the medium solidifies; above its hydrostatic limit, the medium must be treated as non-hydrostatic [66,84]. The resulting non-hydrostatic stress can be accompanied by pressure gradients across the sample chamber [85]. Consequently, the pressure determined by a local pressure marker or probe may depend on its position and local stress state, rather than representing a spatially uniform pressure throughout the sample chamber [85]. Temperature variation and loading-path-dependent effects can further affect the reproducibility of the pressure response and the interpretation of a pressure scale [86,87]. In practice, pressure-medium solidification, non-hydrostatic stress, spatial pressure gradients, temperature variation, and loading-path hysteresis make the pressure

measurand difficult to define and reproduce, causing the measured response to depend on the local sample environment, the selected pressure scale, and its calibration model [85–88]. Systematic differences may therefore occur among pressure scales in their overlapping pressure ranges. Future work should establish systematic cross-comparisons among pressure scales under controlled pressure-medium, temperature, and loading conditions; develop measurement models capable of distinguishing the hydrostatic pressure component from deviatoric stress; and provide complete uncertainty evaluations that include calibration, spectral or structural fitting, temperature effects, stress gradients, hysteresis, repeatability, and residual model errors. In parallel, emerging local pressure-sensing methods, such as NV-center ODMR, should be developed through traceable calibration against reference pressures and validated uncertainty budgets before they can contribute to a reliable SI-linked extreme-pressure measurement route. The relationships among pressure realization, value dissemination, and pressure determination in the ultra-high-pressure and extreme-pressure regimes are summarized schematically in Figure 2.

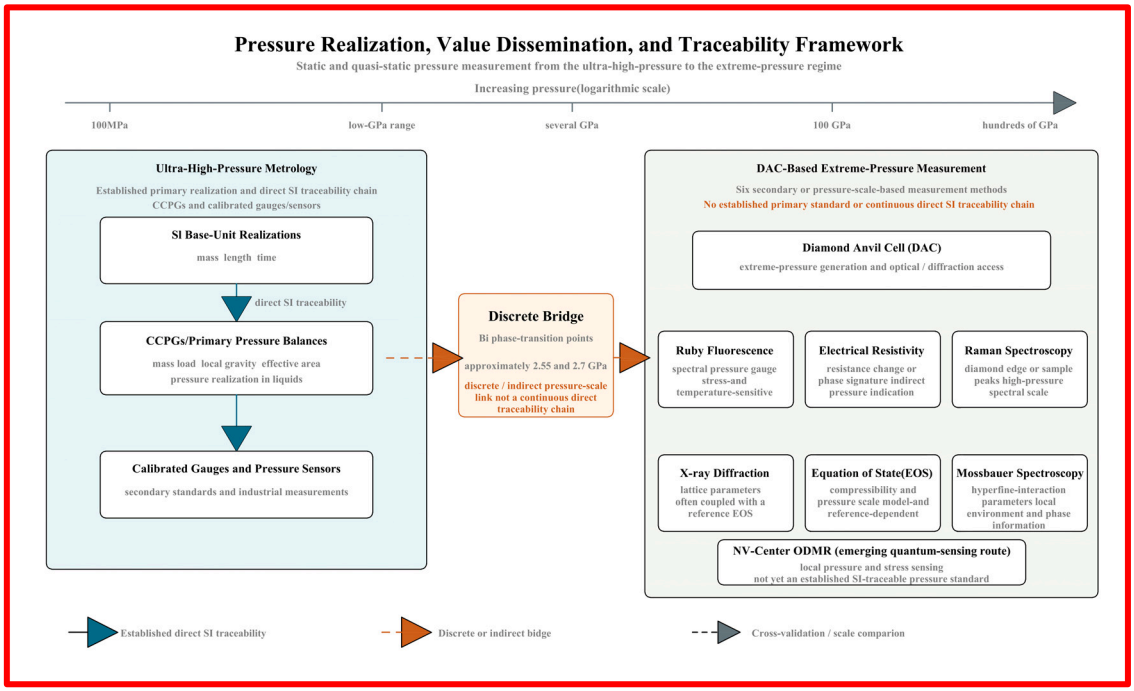


Figure 2. Schematic of pressure realization and value dissemination in the ultra-high-pressure regime, and pressure determination in the extreme-pressure regime.

3. Ultra-High-Pressure Metrology

3.1. Primary Standards for Static and Quasi-Static Ultra-High-Pressure Measurement

Piston gauges are important primary pressure standards for achieving pressure traceability to the SI in the Static and Quasi-Static ultra-high-pressure range. According to differences in piston structure, they can be classified as simple piston gauges, re-entrant piston gauges, and CCPGs, whose basic structures and operating principles are shown in Figure 3 [52]. Among them, CCPGs offer advantages such as a high measurement range, strong reliability, and low measurement uncertainty and are therefore widely used in ultra-high-pressure metrology. National metrology institutes in several countries have adopted CCPGs as one of the core reference standards for ultra-high-pressure traceability [89–101].

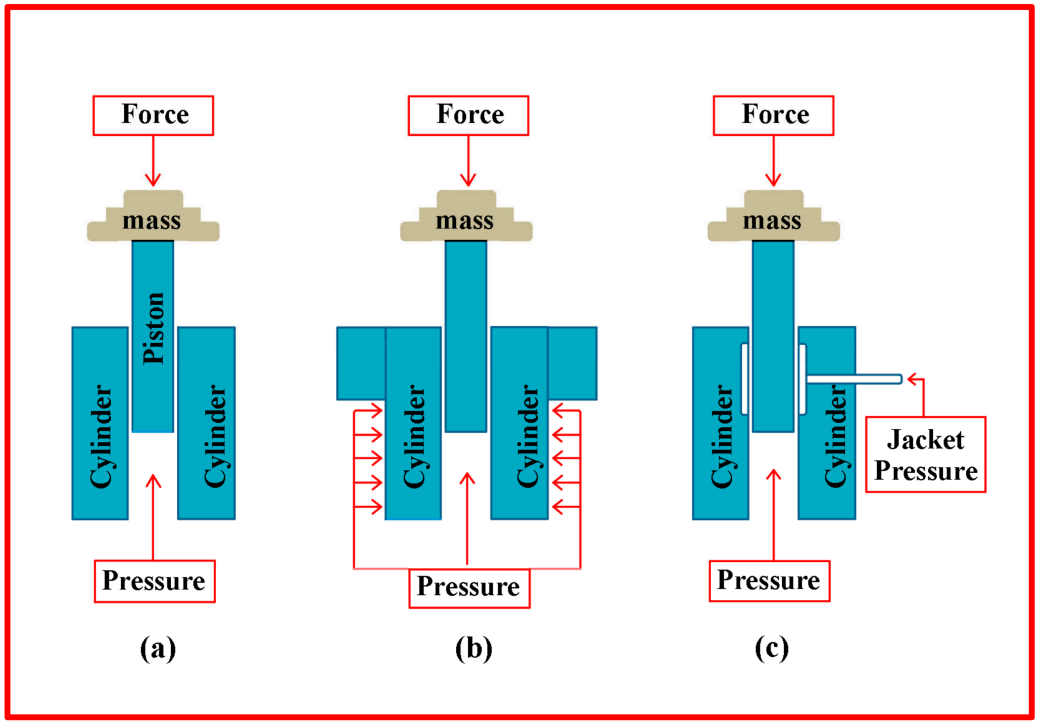


Figure 3. Classification and working principle of piston gauges: (**a**) simple; (**b**) re-entrant; (**c**) controlled-clearance.

Based on conventional piston gauges, a CCPG applies an independent jacket pressure to the outer wall of the piston cylinder to control the clearance between the piston and the cylinder, thereby increasing the operating range of the gauge and reducing the measurement uncertainty caused by variations in the effective area. Taking a controlled-clearance piston with a maximum measurement range of 1500 MPa as an example, its operating principle is shown in Figure 4, and the PCA structure is shown in Figure 5 [91,102].

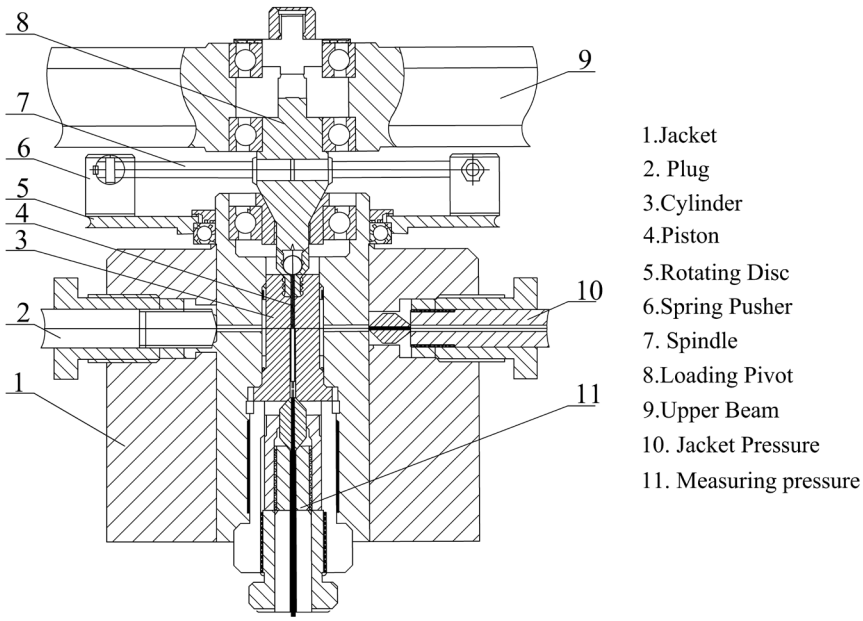


Figure 4. Schematic of the CCPG with maximum pressure 1500 MPa.

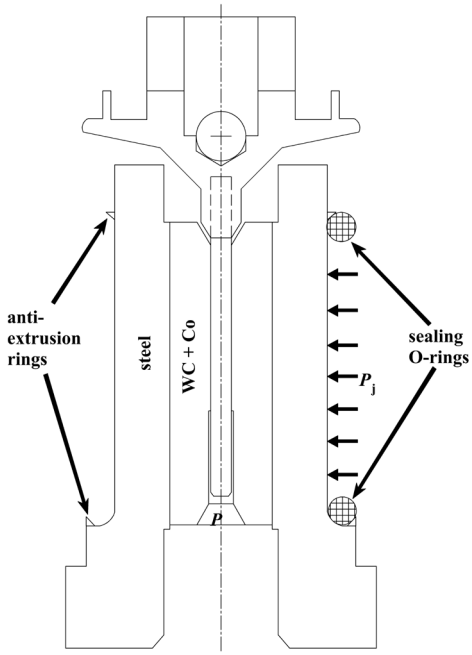


Figure 5. Schematic of the PCA of the CCPG with maximum measuring pressure 1500 MPa.

Because of the introduction of jacket pressure and the non-negligible effects of material deformation under ultra-high-pressure conditions, pressure calculation for a CCPG differs from that for conventional piston gauges and must include correction terms for piston deformation, area expansion, and the nonlinear variation of the effective area. The pressure calculation formula for a CCPG is given as follows [102]:

$$P_m = \frac{mg_L(1-\rho_a/\rho_m)}{A_0(1+bP_0)[1+(a_p+a_c)(T-20)][1+\int_{P_j}^{P_z} d(P_j)dP_j]} \quad (1)$$

where P_m is the pressure to be measured (MPa); m is the total mass of the weights (kg); g_L is the gravitational acceleration (m/s^2); ρ_a is the air density (kg/m^3); ρ_m is the density of the weight material (kg/m^3); A_0 is the effective area of the piston (m^2); b is the relative change in A_0 with respect to the pressure to be measure (MPa^{-1}); P_0 is the pressure to be measured without considering piston deformation (MPa); α_p and α_c are the thermal expansion coefficients of the piston and cylinder, respectively (°C^{-1}); T is the operating temperature of the pressure gauge (°C); P_j is the actual jacket pressure (MPa); P_z is the zero-clearance jacket pressure corresponding to a zero piston fall rate at the pressure to be measured (MPa); and $d(P_j)$ is the relative change in A_0 caused by variation in the jacket pressure (MPa^{-1}).

The above traceability route is established under static or quasi-static equilibrium conditions, where the pressure can be maintained sufficiently long for the piston-load system to reach a stable operating state. Dynamic pressure measurements, in which the pressure varies rapidly with time, require different primary measurement principles and are discussed in the following section.

3.1.1. Development of CCPGs

In 1953, Johnson et al. [103] developed the first CCPG, with a maximum measurement range of approximately 827 MPa and a measurement uncertainty of 0.7%. With the growing demand for metrology in the ultra-high-pressure field, research teams led by Johnson [76] and Nishibata et al. [104] successively proposed several key improvements to CCPGs in the mid-to-late twentieth century, including the use of higher-hardness materials for piston

fabrication to reduce piston deformation under high-pressure conditions and the use of two pressure-transmitting media within their respective optimal pressure ranges, which significantly extended the measurement range and reduced measurement uncertainty. In 2008, Gu et al. [105] selected a high-strength material, YG-8 tungsten carbide, and reduced the measurement uncertainty to 0.02% at 1500 MPa. Hong et al. [102] comprehensively considered the effects of gravity, thermal expansion, piston/cylinder deformation, and jacket pressure and verified the applicability of the Heydemann–Welch model under ultra-high-pressure conditions. Yue et al. [91] accurately determined the zero-pressure effective area of the piston through three sets of cross-float comparison experiments, obtained the piston distortion coefficient and jacket distortion coefficient, and achieved a measurement uncertainty of 0.044% at 1000 MPa.

With the continuing growth of ultra-high-pressure metrology demands across various fields, conventional CCPGs face several challenges when being further extended to higher pressure ranges, including insufficient material strength, complex piston structures, and high manufacturing difficulty. To address these issues, researchers proposed the concept of a pressure multiplier. By mechanically coupling low-pressure and high-pressure piston systems and using the area-ratio principle, a relatively low pressure applied at the low-pressure end can generate an ultra-high-pressure output at the high-pressure end, thereby simplifying the system structure and improving metrological stability. The operating principle is shown in Figure 6. From 2014 to 2025, Sabuga et al. [62,106] developed pressure multipliers with maximum measurement ranges of up to 1600 MPa to extend the range of pressure standards. Through accurate determination and calculation of the zero-pressure effective area and pressure distortion coefficient, as well as optimization of the weight system, the measurement uncertainty was further reduced.

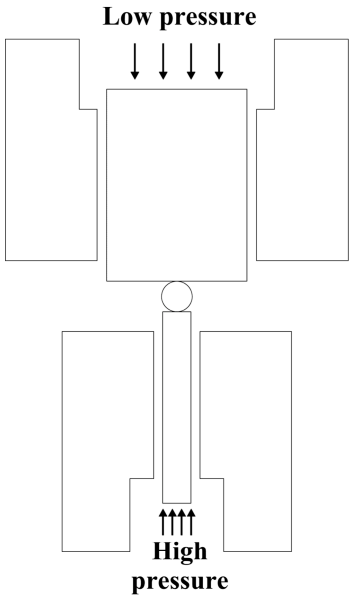


Figure 6. Operation principle of a pressure multiplier.

The development history of CCPGs is summarized in Table 1. More fundamentally, the technological evolution summarized in Table 1 has been driven by the progressive coupling of mechanical and metrological effects at increasing pressure. As the operating pressure increases, piston-cylinder deformation, pressure distribution and fluid flow within the piston-cylinder clearance, pressure-medium viscosity, and sealing reliability increasingly affect the effective area of the PCA. Consequently, the effective area can no longer be treated as a stable geometric quantity, and improvements in material strength or maximum pressure

capacity alone are insufficient to ensure accurate pressure realization. Initially, CCPG development focused on establishing controlled-clearance operation and reducing friction through external jacket-pressure regulation, axial-thrust compensation, and piston rotation. Subsequently, stronger materials, prestressed structures, improved sealing systems, and pressure media selected for high-pressure operation were introduced to increase the usable pressure range and operating stability. More recently, deformation models, jacket-pressure corrections, and pressure-multiplier systems have been used to transform high-pressure generation into traceable pressure realization and dissemination. Critically, the maximum reported operating range in Table 1 is not, by itself, a sufficient indicator of metrological capability: the historically reported 2.6 GPa operating range and the lower ranges of more recent high-accuracy systems should not be compared directly without considering their correction models, operating conditions, and uncertainty budgets. Thus, the central challenge is no longer simply to generate a higher pressure but to demonstrate that the generated pressure remains reproducible, quantitatively characterized, and traceable.

Table 1. The development history of CCPGs.

Ref.	Year	Authors Institution	Main Contribution/Innovation	Maximum Range (MPa)	Measurement Uncertainty (%)	Key Design Technologies	Pressure-Transmitting Medium
[103]	1953	Johnson & Newhall	First proposed the controlled-clearance piston design, in which an external pressure was applied to adjust the sleeve clearance and reduce errors caused by elastic deformation.	≈827	0.7	1. Steel piston and sleeve; 2. Bridgman unsupported seal	Mixture of glucose, glycerin, and water
[76]	1967	Johnson & Heydemann	Introduced axial-thrust compensation for sleeve stress and calculated the relationship between axial thrust and sleeve stress.	2600	0.24	1. Tungsten carbide piston with a diameter of 0.2 cm; 2. Steel tapered sleeve; 3. Independent jacket-pressure system	I-amyl alcohol
[104]	1980	Ken Nishibata et al./NRLM, Japan	Introduced a rotation mechanism to reduce friction and improve sensitivity.	2000	0.023	1. Tungsten carbide piston with 7% Co; 2. 18% nickel maraging-steel sleeve; 3. Elastic-thrust rotation mechanism; 4. Jacket-pressure feedback control	1. White gasoline 2. Di-ethyl-hexyl sebacate
[105]	2008	Gu Shijie et al./SIMT, China	Used YG-8 tungsten carbide, optimized cylindricity through precision lapping, and adopted an 80° conical seal.	1500	0.02	1. YG-8 tungsten carbide piston; 2. Double-layer shrink-fitted prestressed cylinder; 3. Hydraulic weight loading	Glycerol–ethylene glycol mixture
[106]	2014	Sabuga & Haines (PTB/Fluke)	Optimized the sleeve taper and multilayer support structure using finite-element analysis and achieved high-accuracy pressure transfer based on the hydraulic multiplication principle.	1600	0.02	1. Tungsten carbide piston with 6% Co; 2. Independent jacket-pressure system	1. di(2-ethylhexyl) sebacate (DHS) 2. polydiethyl-siloxane (PES-1)

Table 1. *Cont.*

Ref.	Year	Authors Institution	Main Contribution/Innovation	Maximum Range (MPa)	Measurement Uncertainty (%)	Key Design Technologies	Pressure-Transmitting Medium
[90]	2017	Sabuga et al./PTB, LNE, METAS, etc.	Developed a 1.6 GPa hydraulic pressure-multiplier system and combined nonlinear finite-element analysis with multi-material elastic–plastic deformation modeling to establish high-accuracy transfer standards and industrial calibration capability.	1600	0.05	1. 1.6 GPa piston-multiplier structure; 2. Deformation prediction model for high-pressure tubing; 3. Reliability validation of ultra-high-pressure components	50 vol% DHS + 50 vol% petroleum mixture
[102]	2018	Bian Hong et al./SIMT, China	Investigated and determined the linear relationship between jacket pressure and measured pressure for a 1500 MPa controlled-clearance piston gauge.	1500	0.02	1. Pressure calculation based on the H-W model; 2. High-precision components and measurement system	Glycerol–ethylene glycol mixture
[91]	2019	Jin Yue et al./NIM and PTB	Characterized a new 1 GPa PCA and verified a nonlinear correction model for the pressure distortion coefficient.	1000	0.044	1. Double-layer steel sleeve with shrink-fitted prestress; 2. Radial-deformation compensation using jacket pressure; 3. Finite-element validation of contact stress distribution	DHS
[62]	2025	Sabuga et al./PTB	Realized a liquid pressure standard from 0.5 MPa to 1.6 GPa and enabled high-accuracy measurements at different pressure points within this range.	1600	$\leq$0.013	1. Separated dual pressure-balance structure; 2. HP cylinder supported by a shrink-fitted sleeve	1. DHS 2. Mixture 50 vol% DHS and 50 vol% petroleum 3. Mixture 50 vol% glycerol and 50 vol% ethylene glycol

3.1.2. Recent Progress in Key Technologies

Key technological advances in CCPGs have mainly focused on three aspects: uncertainty reduction, range extension, and optimization of operating systems and calibration procedures. Among these, uncertainty reduction centers on the determination of the effective area of the piston; range extension mainly depends on improvements in high-strength PCA, ultra-high-pressure sealing structures, and the performance of pressure-transmitting media; and optimization of operating systems and calibration procedures focuses on jacket-pressure control, assessment of piston operating status, automated calibration, and reduction of human error. Together, these three aspects determine the measurement capability, stability, and reliability of pressure dissemination for CCPGs in the ultra-high-pressure range.

- Uncertainty Reduction: In a CCPG, the pressure value is jointly determined by the applied load and the effective area of the piston; therefore, effective-area determination is a key factor affecting measurement uncertainty. For the measurement of piston effective area, Sanjid et al. [107] proposed the use of two linear variable differential transformers and a displacement laser interferometer to accurately measure the effective piston area, achieving a uncertainty of 56 nm. Stoup et al. [108] developed an ultra-high-precision laser micrometer for measuring the diameters of cylinders and spheres, with a measurement uncertainty of less than 20 nm over a

range of 0.02–55 mm. Reducing the uncertainty in zero-pressure piston effective-area measurement lays the foundation for reducing pressure-measurement uncertainty. However, under ultra-high-pressure conditions, CCPGs must account for multiple factors, including elastic deformation of the PCA, the pressure distribution in the piston–cylinder clearance, jacket-pressure control, temperature variation, piston tilt, and errors in geometric-dimension measurements. Therefore, uncertainty reduction in CCPGs has gradually evolved from simple geometric-dimension measurement to an integrated correction approach combining dimensional metrology, finite-element analysis, and fluid-dynamic modeling.

Sabuga et al. [109] proposed a two-dimensional flow model to calculate the effective area of the PCA, reducing the combined measurement uncertainty by 2% to 70%. Based on elasticity theory and fluid dynamics, Aslanyan et al. [110] established a mathematical model for the pressure distribution in the piston–cylinder clearance, numerically solved the parameter variations under different pressure conditions, as shown in Figure 7, and proposed a piecewise correction strategy, providing a theoretical basis for the design of 1600 MPa-class ultra-high-pressure pistons.

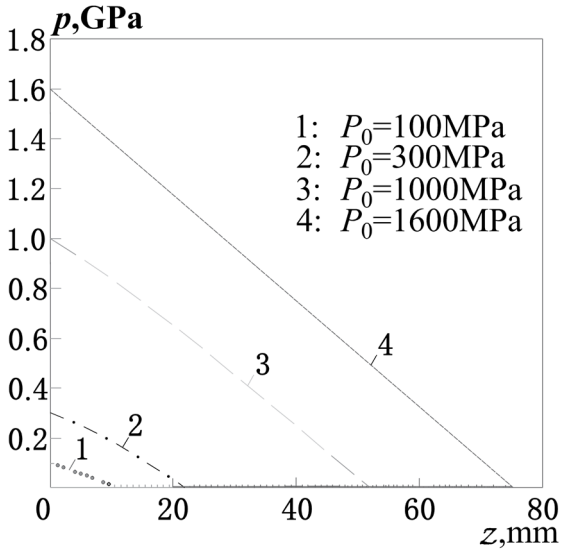


Figure 7. The distribution of pressure p in the gap z of a piston pair for pressures.

Liu et al. [111] proposed a numerical model combining finite-element analysis and fluid dynamics to calculate the elastic deformation of the PCA and the pressure distribution in the clearance under high-pressure conditions. Their model revealed the nonlinear influence of jacket pressure on clearance control and provided a basis for selecting pressure-balance parameters under practical operating conditions. In the finite-element model, the relationship between jacket pressure and the decreasing trend of the PCA outlet clearance width at different measured pressures is shown in Figure 8.

Liu et al. [89] established a two-dimensional axisymmetric finite-element model and a one-dimensional fluid-dynamic model based on a CCPG with a maximum measurement range of 1500 MPa. Through an iterative solution, they accurately obtained the deformation of the PCA and the pressure distribution in the clearance. Wongthep et al. [112] developed an axisymmetric two-dimensional model using the finite-element method and calculated the pressure distortion coefficient, λ, of a 500 MPa free-deformation PCA, thereby optimizing uncertainty evaluation under high-pressure conditions.

These studies indicate that the elastic deformation of the PCA and the pressure distribution in the clearance under ultra-high-pressure conditions exhibit pronounced nonlinear characteristics and that the zero-pressure effective area cannot directly represent the effec-

tive area under operating pressure. Coupled finite-element and fluid-dynamic models are becoming important tools for effective-area determination, pressure-distortion correction, and uncertainty evaluation in CCPGs. Particularly in the GPa pressure range, jacket pressure is used not only to maintain an appropriate piston–cylinder clearance but also as an important variable affecting pressure-dependent correction of the effective area.

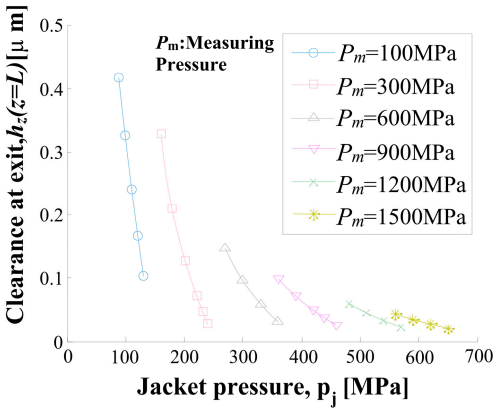


Figure 8. Results near the exit of the piston-cylinder engagement gap are zoomed.

In addition, inherent systematic errors are also important factors affecting the uncertainty of CCPGs. Ginanjar et al. [113] investigated the piston-tilt effect at an ultra-high pressure of 500 MPa, analyzed the influence of piston-rod inclination on the effective area, and used a three-dimensional asymmetric finite-element model to quantify the tilt coefficient associated with changes in effective area caused by piston tilt, as shown in Figure 9. Ginanjar et al. [114] reduced the measurement uncertainty by approximately 37% by exchanging the PCAs of two pressure balances of the same type and averaging the two calibration results, thereby eliminating systematic errors related to mass, temperature, and tilt angle.

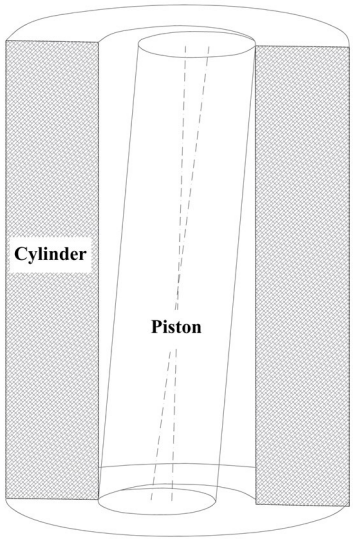


Figure 9. Schematic diagram of the influence of piston inclination on the effective area.

- Range Extension: The range extension of CCPGs is jointly limited by the material strength of the PCA, sealing performance, the properties of pressure-transmitting media, and the structural stability of high-pressure components. As pressure increases, elastic deformation of the PCA becomes more pronounced, stable control of the piston–cylinder clearance becomes more difficult, and the increased viscosity of the

pressure-transmitting medium leads to greater resistance to fluid flow. As a result, the piston fall rate becomes more sensitive to operating conditions such as temperature and rotational speed, thereby reducing the sensitivity and measurement stability of the pressure gauge [115]. At the same time, sealing structures are also more prone to leakage. These factors not only restrict the range extension of CCPGs but also affect their uncertainty to some extent. Therefore, range extension is not merely a matter of increasing pressure-generation capability; rather, it requires coordinated optimization among structural strength, sealing systems, pressure-transmitting media, and the stability of pressure transfer.

Regarding sealing systems, as CCPGs are developed toward higher pressure ranges, sealing failure and leakage directly limit the maximum measurement range and stability of the instrument. Huang et al. [116] proposed a series sealing structure consisting of three groups of sealing rings, each including an O-ring and a Z-shaped sealing ring with grooves on the inner surface, achieving stable rotary sealing under ultra-high-pressure conditions above 100 MPa. Han et al. [117] developed an ultrasonic phased-array measurement system for conical contact and evaluated sealing performance by measuring the contact stress between metal-to-metal sealing surfaces. Yang et al. [118] established a leakage model for the conical sealing structure of pipe joints and investigated the influence of cone angle on conical sealing performance. The conical sealing structure of the pipe joint is shown in Figure 10. The results showed that when the cone angle was 50–60°, the contact pressure was more than twice the yield strength of the sealing material, indicating reliable sealing.

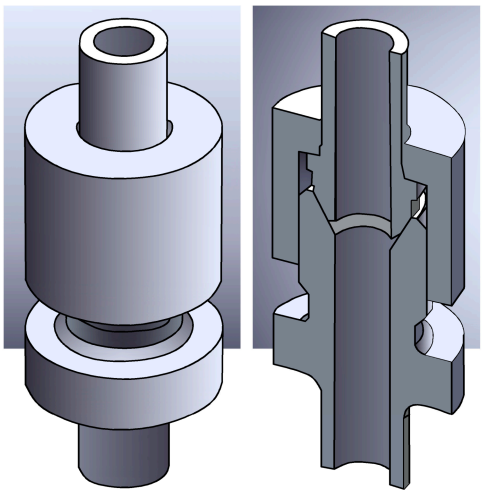


Figure 10. Schematic diagram of the pipeline joint with conical surface seal.

These studies indicate that ultra-high-pressure sealing design has gradually shifted from empirical selection toward a quantitative design stage that integrates contact-stress measurement, leakage modeling, and structural-parameter optimization. For CCPGs, reliable sealing is not only essential for achieving higher pressure output but also directly affects pressure-holding stability and the piston fall rate.

Regarding pressure-transmitting media, the viscosity, compressibility, and high-pressure stability of the medium directly affect the piston fall rate, the pressure distribution in the clearance, and the results of effective-area correction. Yadav et al. [119] experimentally measured piston fall rates under different pressures and with different pressure-transmitting media, analyzed the corresponding characteristic coefficients of the piston for each medium, and found that a mixture of white gasoline, J-13, and sebacate exhibited favorable overall performance under ultra-high-pressure conditions up to 1000 MPa. Sabuga et al. [90] measured the viscosities of di(2-ethylhexyl) sebacate (DHS), polyethyl-

siloxane (PES-1), and a 50% DHS + 50% petroleum mixture at 20 °C under high-pressure conditions using a high-pressure viscometer. On this basis, they constructed a 1600 MPa pressure multiplier with an uncertainty of 0.05% as a transnational ultra-high-pressure standard, laying the foundation for unifying pressure values across European countries. Overall, research on pressure-transmitting media has moved beyond simply screening usable media and is gradually shifting toward measuring high-pressure medium parameters and analyzing piston-motion stability, with the aim of improving pressure–viscosity relationships for different media and identifying optimal pressure-transmitting media under different conditions.

- Optimization of Operating Systems: The National Institute of Standards and Technology developed a fully automated calibration system for piston gauges, using a pressure sensor as a transfer standard together with a dedicated software package. The calibration uncertainty was comparable to that of conventional methods, while the calibration time was substantially shortened, manual data entry was reduced, and the measurement accuracy and stability were experimentally verified [120]. Optimization of the operating system is not merely intended to improve ease of use but to ensure high repeatability, low human error, and stable pressure dissemination in practical CCPG calibration. In future CCPG operating systems, functions such as automatic weight loading, jacket-pressure control, online monitoring of the piston fall rate, automatic correction of environmental parameters, and real-time uncertainty evaluation should be further integrated, enabling CCPGs to evolve from conventional mechanical pressure standards into highly integrated and automated primary pressure standards for ultra-high-pressure metrology.

In summary, the key technological advances in CCPGs can be categorized into three aspects: uncertainty reduction, range extension, and operating-system optimization. These aspects do not develop independently but progress through their mutual interactions. Further development of CCPGs will require the integration of high-strength piston–cylinder materials, coupled fluid-dynamic models, ultra-high-pressure sealing structures, pressure-transmitting-medium databases, and automated calibration systems, thereby forming a primary ultra-high-pressure standard system with a higher measurement range, lower uncertainty, and improved stability.

3.2. Primary Standards for Dynamic Ultra-High-Pressure Measurement

In the static and quasi-static pressure measurements discussed above, pressure can generally be maintained at a stable level or varied slowly, such that the measurement result can be represented by a single pressure value. However, in applications involving combustion instability, blast shock waves, rapid compression, and high-speed fluid machinery [121–124], pressure may exhibit transient characteristics such as rapid steps, short-duration pronounced increases, or periodic fluctuations. The amplitude, rise time, duration, and waveform of such pressure variations must be compatible with the dynamic response of the sensor and measurement chain; otherwise, amplitude distortion, timing errors, or other measurement errors may be introduced [125,126]. Dynamic pressure metrology therefore requires not only the determination of the amplitude and temporal characteristics of the transient pressure history but also accurate characterization of the dynamic response of the measurement system to ensure that the measured signal reliably represents the pressure process of interest [127,128].

Existing methods for dynamic-pressure generation and calibration include drop-weight-based dynamic-pressure standards, shock tubes and diaphragmless shock tubes, and periodic pressure generators driven by pistons or piezoelectric actuators [43,127–130]. In a drop-weight system, a falling mass impacts a piston connected to a hydraulic chamber,

thereby generating a millisecond-scale transient pressure pulse in a liquid medium. This approach is currently one of the important primary metrological routes capable of covering dynamic pressures above 100 MPa [43]. Shock tubes, especially diaphragmless shock tubes, can generate pressure steps with very short rise times and are suitable for the calibration of dynamic pressure transducers and the evaluation of their transient-response characteristics [127]. At present, diaphragmless shock tubes for which primary dynamic-calibration methods have been established mainly operate in the MPa-to-tens-of-MPa range [131]. Recent studies have optimized valve-opening speed, driver-gas conditions, and tube diameter to improve shock formation and propagation, pressure waveforms, and repeatability in diaphragmless shock tubes [131–134]. In particular, shock-wave focusing can directly intensify the shock wave and increase the end-wall pressure, indicating that shock-tube-based systems may become an important route for ultra-high-pressure dynamic-pressure generation and primary metrology in the future [131]. Periodic piston-driven pressure generators are used for periodic dynamic-pressure calibration at controlled frequencies; their attainable pressure amplitude is governed by the piston displacement and area, the bulk modulus of the liquid, and the initial chamber volume, while their usable frequency range is constrained by the mechanical design of the excitation system [135].

3.2.1. Drop-Weight-Based Primary Standards for Ultra-High-Pressure Dynamic Measurements

A drop-weight-based dynamic pressure standard is a primary method for realizing short-duration, high-amplitude pressure pulses in a hydraulic medium through mechanical impact [43]. In contrast to static piston gauges, which maintain stable pressure through a constant load, a drop-weight system generates a time-varying transient pressure pulse through a controlled impact event. It can therefore be used to calibrate the peak and transient responses of dynamic pressure transducers and to provide a traceability basis for evaluating the associated dynamic measurement uncertainty [43,136].

A typical drop-weight dynamic pressure apparatus consists mainly of a drop weight, a piston, a cylinder, and associated structural components, as shown in Figure 11a [137]. During a test, a drop weight of known mass is released from a prescribed height and impacts a piston connected to the hydraulic chamber. The momentum of the drop weight is transmitted through the piston to the confined hydraulic medium, generating a millisecond-scale pressure pulse in the measurement chamber. The resulting pressure waveform is approximately half-sinusoidal, as shown in Figure 11b [137]. Its peak amplitude, rise time, and pulse duration depend on factors including the drop-weight mass, impact velocity, piston dimensions, and elastic modulus of the hydraulic medium [138,139].

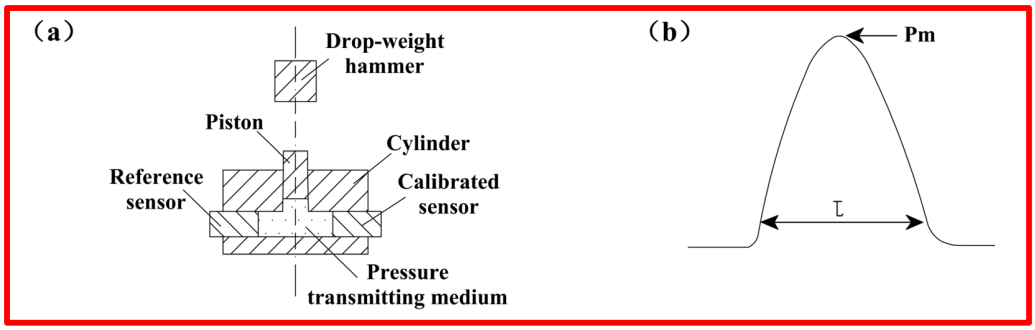


Figure 11. (**a**) Principal diagram of the drop-weight device. (**b**) Half-sine pressure signal.

Similar to a piston gauge, a drop-weight system determines the instantaneous pressure from the ratio of the instantaneous force to the effective area [139]. The force can be determined from the mass of the drop weight and its motion during impact, whereas the

effective area must be evaluated by considering the piston geometry, pressure-induced deformation, and pressure-dependent changes in the effective area [43]. The uncertainty evaluation should also account for the drop-weight mass and acceleration measurements, the effective piston–cylinder area, the compressibility of the hydraulic medium, and the elastic deformation of the system. Mechanical vibrations, spatial pressure non-uniformity during pressure-pulse propagation, and disturbances to the measurement chain caused by sensor installation should also be evaluated according to the apparatus design and measurement location [43,138]. Therefore, a drop-weight-based dynamic pressure standard cannot be treated simply using the static load–pressure relationship; a dynamic model describing the impact and pressure-transmission processes must be established, together with a complete uncertainty budget. Högström et al. [43] developed a drop-weight-based primary standard for dynamic pressure covering approximately 10–400 MPa, with a typical relative expanded uncertainty of 1.5%. Subsequently, Högström et al. [140] proposed a new design incorporating an air-bearing-guided drop weight to reduce lateral friction and guiding errors during drop-weight motion. The apparatus generated millisecond-scale half-sinusoidal pressure pulses with a maximum dynamic pressure of approximately 500 MPa. Based on the preliminary experimental results and uncertainty budget, a relative expanded uncertainty of 0.9% (k = 2) was achieved.

A drop-weight-based dynamic pressure standard can generate high-amplitude transient pressure pulses in a hydraulic medium and is therefore particularly suitable for the dynamic calibration of high-range hydraulic pressure transducers [136]. However, its output is a pressure pulse of finite duration rather than an ideal pressure step with an independently controllable rise time. The pressure history is influenced by the impact process, the compressibility of the hydraulic medium, and the elastic response of the piston–cylinder assembly and pressure chamber [43,138]. Accordingly, this method is particularly suitable for the calibration of high-amplitude, millisecond-scale transient pressures. For the evaluation of steeper pressure steps or dynamic responses with higher bandwidths, it can be used complementarily with shock-tube methods [127]. Future work should improve the repeatability of the pressure pulses, characterize the pressure-field uniformity at the sensor mounting location, strengthen the evaluation of dynamic measurement uncertainty, and extend the calibration capability to different types of ultra-high-pressure transducers.

3.2.2. Shock-Tube-Based Primary Calibration Methods for Dynamic Pressure Measurements

In addition to drop-weight systems, shock tubes are widely used physical excitation devices in dynamic pressure metrology, particularly for characterizing the response of pressure transducers to rapid pressure steps [141]. A conventional shock tube generally consists of a high-pressure driver section and a low-pressure driven section separated by a diaphragm, as shown in Figure 12 [142]. Upon diaphragm rupture, the driver gas expands rapidly and generates a propagating shock wave in the driven section. When the shock wave reaches and reflects from the end wall, a step-like pressure signal with a very short rise time is generated in the vicinity of the end wall. Consequently, shock tubes can be used to investigate the rise time, high-frequency response, and dynamic sensitivity of pressure transducers [143,144].

It should be noted that the ability to generate a pressure step does not, by itself, qualify a shock tube as a primary dynamic pressure standard. For a shock tube based on a gas-dynamic model, the model assumptions must be validated, and the amplitude of the reflected-shock pressure step must be calculated using traceably measured shock-wave velocity, the initial absolute pressure and temperature of the driven gas, and relevant thermophysical properties of the gas. A corresponding uncertainty evaluation must also be

completed. Only when these conditions are fulfilled can a shock tube serve as a primary dynamic-pressure calibration method [145].

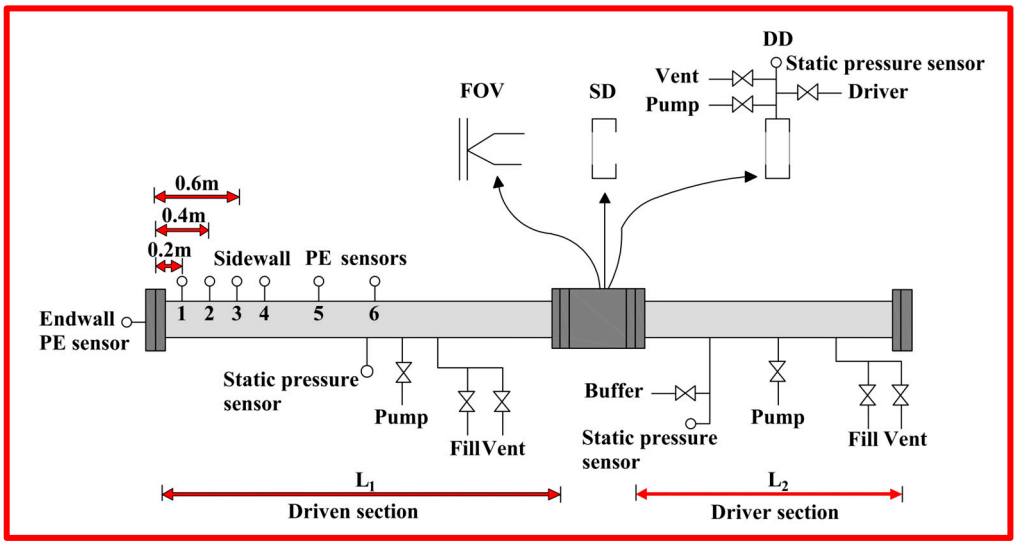


Figure 12. Schematic illustration of the shock tube. FOV, fast-opening valve; SD, single diaphragm; DD, double diaphragm.

In conventional shock tubes, the material properties and rupture behavior of the diaphragm affect shock formation and may introduce substantial uncertainty in the repeatability of the generated shock wave. Incomplete diaphragm rupture may also produce a pressure-step amplitude lower than that predicted by ideal shock-tube theory, while solid fragments generated during rupture may contaminate or damage the pressure transducer under calibration. Diaphragmless shock tubes replace the diaphragm with a fast-opening valve, thereby eliminating diaphragm replacement and the associated assembly procedures after each test, as well as the potential influence of diaphragm fragments on the test section and pressure transducers. Nevertheless, the valve-opening speed and opening mechanism affect shock formation and the pressure waveform; their dynamic characteristics must therefore be characterized and evaluated [132,145]. Svete and Kutin [127] investigated the primary dynamic-calibration characteristics of a diaphragmless shock tube and demonstrated its applicability to the traceable calibration of dynamic pressure transducers. However, the opening speed and opening process of the fast valve, as well as mechanical vibrations of the apparatus, can still affect shock formation and the resulting pressure waveform; these factors should therefore be considered explicitly in the uncertainty evaluation of diaphragmless shock tubes. More recently, research on diaphragmless shock tubes has expanded from improving waveform repeatability to increasing the attainable pressure amplitude. Valve-opening characteristics, driver- and driven-gas combinations, and tube-geometry parameters have all been investigated to improve shock formation and propagation. In particular, the introduction of shock-wave-focusing structures can directly increase the pressure amplitude at the end wall. Svete et al. [131] used two focusing elements to transform a planar shock wave into a converging shock wave, experimentally obtaining end-wall pressures of 13.4 MPa and up to 44 MPa, respectively. With further advances in shock-wave focusing, fast-valve technology, and waveform characterization, diaphragmless shock tubes may become an important future route for ultra-high-pressure dynamic-pressure generation and sensor calibration.

3.3. Secondary Pressure Standards for Ultra-High Pressure

Ultra-high-pressure secondary pressure standards directly provide pressure readings through changes in the resistance, capacitance, frequency, or optical signals of pressure-sensitive elements under applied pressure. They are the main tools for high-pressure measurement in engineering applications, and their values are usually traceable to the SI after calibration against CCPGs [146]. These instruments mainly include pressure gauges and pressure sensors.

Ultra-high-pressure gauges were developed relatively early, and their structural design and materials are comparatively mature, with high reliability and wide application. The main challenges at present are that under extreme environmental conditions such as high temperature, high pressure, and strong radiation, manual reading is difficult and subject to significant observer error, making it difficult to meet the metrological requirements of modern engineering for high accuracy and high reliability. Therefore, intelligent recognition technologies have been investigated for pointer pressure gauges, including template-matching methods [147], OpenCV-based image-processing methods [148], and deep-learning-based image-processing methods [149]. Meanwhile, digital pressure gauges, through signal conditioning and digital display modules, can effectively avoid reading errors caused by viewing-angle deviation, nonuniform illumination, and observation distance and therefore show promising development potential.

Ultra-high-pressure sensors commonly use physical mechanisms such as piezoresistive response, strain-induced electrical variation, and resonant-frequency shifts to convert externally applied ultra-high pressure into measurable electrical signals, thereby enabling high-accuracy pressure detection. According to the type of pressure-sensitive element, they can be classified into piezoresistive sensors, resonant sensors, optical sensors, and other types.

Piezoresistive sensors use the strain generated in a pressure-bearing structure under applied pressure to induce resistance changes in piezoresistive elements, which are then converted into voltage signals through circuits for pressure measurement. Owing to their relatively simple structure, fast response, and ease of integration, they are currently one of the commonly used approaches for ultra-high-pressure engineering measurements above 1000 MPa [150]. However, their measurement range is limited by diaphragm strength, stress concentration, and packaging reliability. Zhao et al. [151] combined a silicon-on-insulator (SOI) piezoresistive chip with a high-strength elastic structure, avoiding direct pressure loading on a conventional diaphragm structure; instead, controllable strain was generated by the elastic body and read out by the piezoresistive elements, achieving a measurement range of up to 1600 MPa. Zhang et al. [152] used a truncated-cone structure to regulate stress distribution and alleviate local stress concentration under ultra-high pressure and combined it with an SOI piezoresistive chip to achieve measurements over a 1600 MPa range and in high-temperature environments up to 800 °C. Sinha et al. [153] used the high surface-area-to-volume ratio, excellent mechanical properties, and miniaturized membrane structure of graphene to improve sensitivity per unit area, providing a new perspective for nanoelectromechanical systems (NEMS)-based ultra-high-pressure sensing.

Resonant sensors measure pressure through pressure-induced changes in resonant frequency. Taking quartz resonant pressure sensors as an example, quartz exhibits favorable frequency stability, mechanical quality factor, and temperature characteristics, making it suitable for high-accuracy pressure measurement. Zhang et al. [154] designed a high-accuracy and high-stability quartz resonant ultra-high-pressure sensor by using a pressure cylinder and a flexible lever as the pressure-conversion unit, together with dual quartz double-ended tuning fork resonators as the differential-output resonant unit. Subsequently, the same research team further adopted an integrated push–pull pressure-conversion struc-

ture made of beryllium copper and upgraded the resonant unit to a pure axial-loading push–pull differential configuration, which further suppressed common-mode interference and eliminated nonuniform stress in the tuning forks. Together with optimized fabrication and packaging processes, these improvements significantly enhanced sensor performance [155]. Qian et al. [156] integrated the dual pressure-sensitive mechanisms of diaphragm bending and bulk compression, designed a dual-resonator structure, and achieved temperature self-compensation through differential frequency output. Zhang et al. [157] developed a sandwich-type all-quartz sensing structure using an AT-cut all-quartz sensing element, effectively extending both the pressure-measurement range and the applicable temperature range. Ye et al. [158] adopted bulk-compression sensing and a dual-chamber design to reduce stress, further extending the pressure-measurement range to 180 MPa.

In addition to piezoresistive and resonant sensors, optical sensors measure pressure by converting pressure-induced structural deformation into changes in optical intensity, phase, wavelength, or interference signals. Qi et al. [159] developed a novel ultra-high-pressure optoelectronic sensor by combining a new embedded structure with micro-electro-mechanical systems (MEMS) and optimized the sensor geometry through analyses of its mechanical and optical characteristics. Because signals are transmitted through optical fibers, such sensors are less susceptible to electromagnetic interference and offer good long-distance transmission capability. Sun et al. [160] designed an ultra-high-pressure sensor based on a thick-walled cylindrical π-phase-shifted fiber Bragg grating (π-FBG) and established a finite-element model to optimize the sensor structure and improve analytical accuracy. Owing to the low transmission loss of optical fibers, the ease of miniaturizing sensing heads, and the ability to place the light source and demodulation system away from the high-pressure site, fiber-optic sensors are particularly suitable for complex environments, including deep-sea exploration, petroleum exploration, strong electromagnetic interference, and confined high-pressure chambers. In addition, Hu et al. [161] investigated the charge-transfer behavior and molecular-structure evolution of triboelectric polymers under pressures of 0–500 MPa and fabricated an ultra-high-pressure triboelectric sensor with a safe operating range of up to 160 MPa, providing a new approach for ultra-high-pressure sensing.

In summary, the sensor technologies summarized in Table 2 occupy different positions within the ultra-high-pressure metrology framework. CCPGs remain responsible for primary pressure realization, whereas calibrated sensors are used for pressure dissemination, transfer, and application-oriented measurement. Piezoresistive sensors have achieved GPa-level range extension through SOI piezoresistive chips and pressure-conversion structures. As indicated by their reported ranges in Table 2, they are primarily suited to high-range working measurements in ultra-high-pressure engineering; however, their uncertainty, long-term stability, and dependence on the pressure medium, temperature, and mounting conditions require further improvement. Resonant sensors, in contrast, provide lower reported uncertainties through differential configurations and temperature compensation and are therefore more suitable for high-accuracy secondary measurement or pressure-transfer applications within their presently lower measurement range. Optical sensors provide a complementary role in conditions requiring electromagnetic-interference immunity, remote interrogation, or compact sensing heads, although their traceability depends on the calibration of both the pressure-sensitive structure and the optical interrogation system. Emerging mechanisms, including fiber-optic and triboelectric sensing, further expand the available sensing routes, but their roles as traceable secondary standards will depend on the establishment of stable calibration functions, reproducibility, and complete uncertainty evaluations. Future research should therefore focus not only on improving measurement range, uncertainty, sensitivity, and environmental adaptability, but also on

matching each sensor technology to an appropriate calibration route and metrological role within a traceable secondary pressure-dissemination system.

Table 2. Summary of reported ultra-high-pressure sensors.

Ref.	Sensor Type	Maximum Range (MPa)	Uncertainty (%)	Sensitivity	Operating Temperature (°C)	Structural Features
[151]	Piezoresistive	1600	4.09	Not reported	Not reported	1. Cylindrical elastic body; 2. SOI chip with eutectic bonding
[152]	Piezoresistive	1600	3.74	7.955 mV/GPa	Up to 800	1. Truncated-cone structure; 2. SOI piezoresistive chip; 3. Wheatstone bridge
[153]	Piezoresistive	1000	Not reported	25,000/Pa·m^2	Not reported	1. Graphene membrane array; 2. Multichannel Wheatstone bridge
[154]	Resonant	120	0.0365	27.3 Hz/MPa	−20–60	1. Cylinder and flexible lever; 2. Differential DETF resonators
[155]	Resonant	120	0.0266	46.32 Hz/MPa	−20–60	Integrated push–pull structure
[156]	Resonant	100	0.015	261.10 Hz/MPa	−10–50	1. Dual-resonator structure; 2. Multiple microcavities
[157]	Resonant	120	0.015	365 Hz/MPa	−40–150	1. Sandwich-type all-quartz sensing structure
[158]	Resonant	180	0.042	Resonator I ≈ −180 Hz/MPa, Resonator II ≈ −82 Hz/MPa	50–175	1. Dual-chamber design; 2. Au–Si eutectic bonding and Au–Au thermocompression bonding
[159]	Optical	120	0.079	1.071 rad/MPa	−10–60	1. Embedded MEMS microcavity; 2. Dual-reflection-surface interference
[160]	Optical	120	0.033	5.884 pm/MPa	2–20	1. π-FBG sensing unit; 2. Thick-walled cylindrical substrate

4. Extreme-Pressure Metrology

The pressure traceability system built around CCPGs offers high metrological accuracy and a complete traceability chain. However, owing to material and structural limitations, the current maximum pressure-measurement capability of CCPGs is 2.6 GPa [76]. With the continuous development of science and technology, however, the demand for pressure metrology in fields such as high-pressure materials-property research, geological materials research, and high-pressure physics has extended far beyond the ultra-high-pressure range into the extreme-pressure regime [162–164]. Accordingly, the demand for extreme-pressure measurement is increasing.

4.1. Generation of Extreme Pressure

To simulate extreme-pressure environments in the laboratory, devices capable of generating extreme pressure are required. Diamond anvil cells (DACs) are an ideal choice for achieving extreme pressure because of their excellent hardness and chemical inertness, and their structure is shown in Figure 13 [165]. A DAC generates extreme pressure by applying an external force to a pair of diamond anvils, thereby concentrating the load onto a tiny sample chamber [166,167].

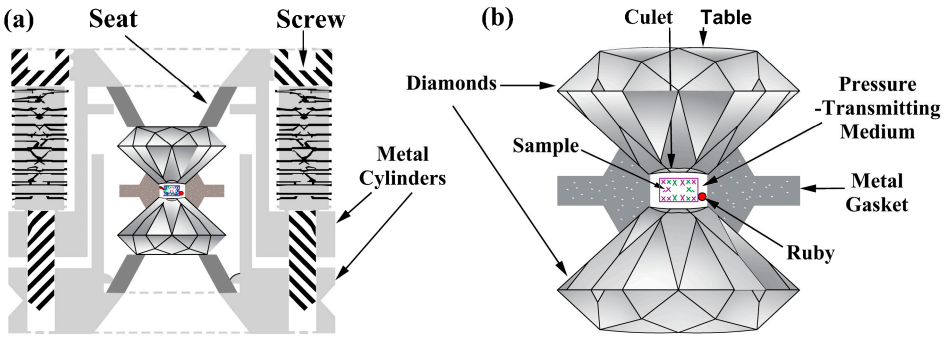


Figure 13. Cross-sectional diagram of DAC: (**a**) cross-sectional view; (**b**) diamond/gasket assembly.

In a DAC, the diamond anvils exhibit high optical transparency over a broad wavelength range [168], allowing photons of different wavelengths to pass through the sample. This enables DACs to be combined with techniques such as X-ray diffraction (XRD), Raman spectroscopy, and Mössbauer spectroscopy to characterize the structure and properties of materials under extreme pressure conditions [169,170]. In addition, DACs can also be coupled with techniques such as electrical resistivity measurement [169], equation-of-state calculations [171], and ruby fluorescence spectroscopy [85] for pressure determination.

4.2. Measurement of Extreme Pressure

In 1977, the first International Practical Pressure Scale (IPPS) task group was established at the 6th International Conference of the Association for the Advancement of High Pressure Science and Technology (AIRAPT) [166]. In the 1980s, this task group proposed the ruby pressure scale, Decker's equation of state for NaCl, and a set of pressure reference points as pressure reference standards [172]. At the end of the twentieth century, the first International Pressure Calibration Workshop proposed several reference points for pressure standards [173]. In 2017, the IPPS task group was established at the 26th AIRAPT Conference, with the aim of constructing a pressure scale that is practical, revisable, and multifunctional. In 2019, a proposal for the ruby pressure gauge was presented at the 27th AIRAPT Conference and was approved by the Executive Committee in June 2020 [85].

As an internationally recognized method for extreme-pressure metrology, the ruby pressure scale has a recommended pressure-measurement range of up to 150 GPa, while ruby-based pressure measurement exhibits relatively large uncertainty above 150 GPa [85]. In addition, ruby is structurally metastable at pressures above 80–100 GPa, and its fluorescence intensity decreases with increasing pressure [174,175]. Under pressure conditions above 150 GPa, the ruby pressure gauge is therefore difficult to use for metrological purposes. In addition to ruby pressure gauges, various extreme-pressure metrology techniques have been developed, as summarized in Table 3. The range and uncertainty information of various measurement methods are shown in Table 4 [62,83,85,109,176]. For DAC-based extreme-pressure measurements, including ruby-fluorescence, diamond-edge Raman, XRD, and EOS-based pressure determinations, the uncertainty evaluation should explicitly account for the actual stress and thermal conditions of each experiment. Pressure-

medium solidification may give rise to non-hydrostatic stress, including deviatoric stress, as well as stress inhomogeneity and spatial pressure gradients; where applicable, these effects should be quantified using ruby-line width and R1-R2 splitting, diffraction-based lattice-strain analysis, or spatial pressure mapping and incorporated into the uncertainty budget [85,176]. Temperature uncertainty, including local laser heating and temperature gradients, should be propagated through the temperature-dependent pressure calibration or EOS [177,178]. In addition, potential loading-path hysteresis should be evaluated by compression-decompression cycles for the specific sample, pressure medium, and pressure scale; the residual after branch-specific correction, or the experimentally observed branch difference when no correction is applied, should be included in the uncertainty budget [179].

The methods listed in Table 3 are complementary rather than mutually substitutable, because their applicability depends on the accessible pressure range, sample characteristics, stress and temperature conditions, and available experimental probes [83,85,176]. Ruby fluorescence is widely used for pressure measurement in optically transparent DACs; however, the IPPS-Ruby2020 scale is proposed only up to 150 GPa at room temperature, and extrapolation to higher pressures may introduce larger uncertainties owing to the weakening of ruby fluorescence and the structural metastability of ruby above 80–100 GPa [85]. Temperature effects and non-hydrostatic stress must also be considered in fluorescence-based pressure determination [85,86]. Electrical-resistivity measurements provide material-specific complementary information on pressure-induced electronic transitions in samples that can be equipped with electrical contacts, rather than serving as a universal pressure scale [180]. When a crystalline reference material and suitable diffraction access are available, in situ XRD coupled with an appropriate EOS can determine pressure from measured unit-cell volumes and can additionally assist in estimating deviatoric stress [85]. At pressures beyond the useful range of ruby fluorescence, the diamond-edge Raman scale provides an alternative pressure-determination route; however, its calibration is affected by the stress state in the diamond anvils and by the cell geometry, gasket material, pressure medium, and sample stiffness [176]. EOS-based pressure values are conditional on the selected reference material and pressure scale, and different scales can yield significantly different pressure estimates [83]. Mössbauer spectroscopy is a composition-specific complementary probe for Fe-bearing materials, since pressure-dependent hyperfine parameters can be used to monitor changes in the valence state, spin state, and crystallographic site of iron [181]. Accordingly, cross-checks between optical pressure gauges and XRD/EOS measurements are valuable for establishing internally consistent pressure values and for evaluating stress conditions in DAC experiments.

In practice, because pressure-induced phenomena involving crystal structures, physical properties, and chemical reactions of materials are highly complex, and because it is difficult to precisely reproduce the same temperature and pressure conditions at extreme pressures of hundreds of GPa, multiple measurement or computational methods are often combined for cross-validation to improve the efficiency, accuracy, and reliability of extreme-pressure metrology [169]. The diversified development of extreme-pressure metrology techniques has enriched available measurement approaches and promoted innovation in metrological theory, but several challenges remain.

Table 3. Extreme-high-pressure metrology technology.

Ref.	Measurement Method	Measurement Principle	Applicable Materials
[85]	Ruby pressure gauge	Relationship between fluorescence peak shift and pressure	Independent of the sample material
[169]	Electrical resistivity measurement	Pressure-induced changes in electrical resistivity	Metals
[182]	X-ray diffraction (XRD)	Pressure determination based on changes in crystal structure and lattice parameters	Crystalline materials
[183]	Raman spectroscopy	Raman shifts related to lattice stress	Carbon materials and minerals
[184]	Equation of state	Pressure inferred from a known equation of state	Known materials with empirical or semi-empirical models
[185]	Mössbauer spectroscopy	Analysis of electronic states through perturbations of nuclear energy levels	Fe-group materials

Table 4. Representative pressure ranges and uncertainty information for ultra-high- and extreme-pressure measurement methods.

Method	Representative Pressure Range	Reported Uncertainty Information	Main Influencing Factors
CCPGs	0.5 MPa–1.6 GPa	Relative standard uncertainty: 0.0005–0.013%	Mass and local gravity; air-buoyancy correction; effective-area evaluation and pressure distortion; thermal and jacket-pressure corrections; and other system-specific factors.
Ruby pressure gauge	Up to 150 GPa at room temperature	Maximum pressure uncertainty: 2.5%	Non-hydrostaticity of the pressure medium and associated pressure gradients
Raman spectroscopy	Ambient pressure to approximately 500 GPa	Raman-edge midpoint localization uncertainty: approximately 1–5.5 GPa up to 400 GPa and 5.5–10 GPa at higher pressures	Raman-edge midpoint determination, stress distribution at the diamond anvils, spatial pressure gradients, and the reference EOS
XRD	Representative experiment up to 477 GPa	P = 477 +/− 21 GPa in a coupled Au-XRD/EOS/Raman experiment	Lattice strain under non-hydrostatic compression, spatial pressure gradients, and the EOS of the reference material
Equation of state	Pressure-scale analysis up to 364 GPa	Pressure-scale variation up to approximately 7% in the room-temperature megabar range	The selected reduced shock-wave EOS and thermodynamic conditions

One of the major challenges in pressure metrology under extreme pressure conditions is how to accurately trace measurement results to the pressure standard in the SI. At present, the historically reported operating range of CCPGs remains below 3 GPa. To extend pressure metrology to higher pressures, the phase-transition pressures of bismuth

(Bi) have become important "bridging points": the Bi-I→Bi-II transition occurs at approximately 2.5 GPa, and the Bi-II→Bi-III transition occurs at approximately 2.7 GPa [186,187]. Bi phase-transition points can serve as discrete reference points linking the upper measurement limit of piston gauges with the low-GPa range of DACs, but they provide calibration anchors only at limited pressure points and are therefore insufficient for forming a continuous traceability chain over higher pressure ranges. As pressure continues to increase, pressure metrology relies on indirect calibration methods, such as pressure estimation using DACs in combination with phase-transition points of reference materials or Raman spectral shifts, with interpolation corrections based on equations of state [182–184]. These methods generally depend on reference materials, empirical or semi-empirical calibration relationships, and equation-of-state models, and their direct traceability chains to the SI unit of pressure remain incomplete, leading to substantial uncertainty and reproducibility issues in metrological results.

In recent years, researchers have begun to move beyond the dependence of conventional extreme-pressure metrology methods on empirical calibration curves and to explore quantum-traceable routes for extreme-pressure measurement. Ryotaro Suda et al. [188] proposed and experimentally demonstrated a quantum pressure-sensing method based on nitrogen-vacancy (NV) centers in nanodiamonds. In this method, nanodiamond particles containing NV centers are dispersed in the sample chamber of a DAC, and laser and microwave excitation are used jointly to measure changes in the splitting of NV spin energy levels under external stress, thereby obtaining optically detected magnetic resonance (ODMR) spectra. Under a specified spin-Hamiltonian model and controlled or independently characterized temperature and magnetic-field conditions, ODMR spectra can be used to infer local pressure and stress components [188–190]. The use of frequency as the primary observable therefore provides considerable potential for establishing an SI-linked pressure-measurement route. However, SI traceability of pressure is not established by frequency measurement alone but requires a calibrated measurement model linking ODMR spectra to a specified pressure measurand and an unbroken, documented chain of calibrations [191]. Reported NV-based high-pressure studies demonstrate the calibration of pressure-frequency coefficients and the need to account for temperature, magnetic-field effects, non-hydrostatic stress, and nanodiamond orientation when interpreting ODMR spectra [188–190]. Accordingly, a future uncertainty budget should include contributions from the reference pressure, resonance-frequency fitting, model coefficients, environmental corrections, spatial stress gradients, repeatability, and residual model error, in accordance with the Guide to the Expression of Uncertainty in Measurement (GUM) framework [192]. Such a complete traceability chain and uncertainty evaluation have not yet been demonstrated for NV-center ODMR at extreme pressure. Unlike conventional methods such as ruby fluorescence and Raman spectroscopy, which rely on empirical fitting functions, this method uses atomic-scale frequency as the measurand and is expected to reduce dependence on traditional empirical calibration curves, providing a theoretical basis for tracing pressure values to frequency. However, this method is still at an exploratory stage and remains some distance from becoming a reproducible, calibratable extreme pressure standard with a complete uncertainty budget. Quantum metrology is gradually becoming a key technology for overcoming bottlenecks in extreme-pressure metrology and provides an important foundation for constructing a full-range quantum traceability chain for pressure.

5. Current Challenges and Future Perspectives

Overall, the development of ultra-high-pressure and extreme-pressure metrology has gradually shifted from technical improvements in individual pressure-measurement instruments toward the improvement of metrological systems involving pressure realization,

pressure dissemination, consistency in pressure calibration, and uncertainty evaluation. CCPGs, pressure sensors, and related instruments support the pressure traceability chain from 100 MPa to the low-GPa range, whereas pressure calibration methods such as ruby pressure gauges, XRD, and Raman spectroscopy extend measurement capabilities to higher pressure ranges. However, unified primary standards and traceability routes are still lacking across different pressure ranges and pressure calibration methods. This section summarizes current challenges and future development directions in terms of primary and secondary ultra-high-pressure standards, DAC-based pressure calibration methods, and quantum pressure sensing.

5.1. Primary and Secondary Pressure Standards for Ultra-High Pressure

CCPGs are currently the core instruments for achieving pressure traceability and pressure dissemination in the ultra-high-pressure range, enabling pressure to be traced to the SI. After long-term development, CCPGs have formed a relatively mature technical system in structural design, jacket-pressure control, effective-area determination, and uncertainty evaluation and can provide stable and reliable pressure references from hundreds of MPa to the low-GPa range. The uncertainty of CCPGs is not dominated by a single factor but is affected by multiple factors, including elastic deformation of the PCA, jacket-pressure control, viscosity changes in pressure-transmitting media under high pressure, ambient temperature, piston tilt, and errors in geometric-dimension measurement. Therefore, finite-element analysis, fluid-dynamic models, and actual calibration experiments need to be combined to comprehensively evaluate the internal fluid–structure interaction state of the PCA, further reduce measurement uncertainty, and provide more stable and reproducible pressure values for ultra-high-pressure metrology.

Various ultra-high-pressure sensors have made significant progress in range extension, environmental adaptability, and new pressure-sensitive mechanisms. From the perspective of traceability, ultra-high-pressure sensors need to be calibrated against CCPGs to establish traceability to the SI. However, the indication corrections obtained during sensor calibration are usually valid only under the corresponding calibration conditions, such as the pressure medium, medium temperature, and mounting state. In practical applications, these conditions may change, leading to zero drift, sensitivity drift, increased hysteresis, or nonlinear errors, and these effects are more pronounced in the ultra-high-pressure range [193–196]. Therefore, as ultra-high-pressure sensors continue to develop toward lower uncertainty and higher measurement ranges, segmented calibration methods for different pressure ranges, loading paths, and environmental conditions should be improved in combination with ultra-high-pressure primary standards.

5.2. Multiple Pressure Standards for Extreme Pressure

Multiple pressure-measurement methods have been developed for the extreme-pressure range, but their traceability chains remain incomplete. Pressure-induced phase-transition points of materials such as bismuth can serve as discrete pressure reference points calibrated against primary pressure standards and can be used to connect mechanical pressure standards with high-pressure experimental devices; however, their applicability is affected by factors such as temperature, hydrostaticity, phase-transition criteria, hysteresis effects, and uncertainties in material phase diagrams [81,197–200]. Therefore, in the near term, extreme-pressure measurement will still need to rely on cross-validation using DACs and multiple pressure-measurement methods. Ruby fluorescence, Raman spectroscopy, XRD, phase-transition points, and equations of state are not mutually substitutable methods; rather, they provide pressure information under different pressure ranges, sample systems, and experimental conditions. In the future, the consistency among these pressure

scales should be further improved, and a segmented traceability route should be established from the low-GPa range covered by CCPGs, through phase-transition reference points such as Bi and DAC-based pressure scales, to the extreme-pressure range above hundreds of GPa, thereby further improving the comparability and credibility of extreme-pressure measurement results.

5.3. Quantum Pressure Sensing

Quantum pressure sensing provides a new direction for improving pressure metrology systems under extreme pressure conditions. Among emerging approaches, pressure sensing based on nitrogen-vacancy centers (NV centers) in diamonds has attracted increasing attention in recent years. NV centers possess spin energy-level structures that can be read out by ODMR, and these energy levels are affected by factors such as stress and strain, temperature, magnetic fields, and electric fields [201–205]. Under high-pressure conditions, local stress and strain alter the spin Hamiltonian of NV centers, resulting in changes in the ODMR resonance frequency, zero-field splitting, or spectral-line splitting. By measuring these frequency signals and combining them with stress-coupling models and calibration relationships, the local pressure and stress state can be inferred [84,206–208]. Compared with conventional methods such as ruby fluorescence and Raman spectroscopy, the core measurand in NV-center pressure sensing is frequency, which has a well-established basis for SI traceability; therefore, this approach has theoretical potential for development into a quantum pressure-sensing method [209]. However, NV-center pressure sensing is still at the exploratory and developmental stage and remains some distance from becoming a mature pressure standard for extreme pressure. With continued advances in quantum pressure-sensing technologies, it is expected to gradually support the construction of a unified pressure metrology system covering the range from ultra-high-pressure to extreme pressure.

6. Conclusions

This review has examined ultra-high-pressure and extreme-pressure metrology technologies and their traceability systems. At present, CCPGs remain the core instruments for establishing SI traceability in static and quasi-static ultra-high-pressure metrology, whereas drop-weight-based primary standards provide an established route for dynamic ultra-high-pressure metrology. Pressure multipliers provide an important means for pressure dissemination over higher liquid-pressure ranges, and ultra-high-pressure gauges and pressure sensors are used for engineering field measurements and process monitoring. Together, these instruments constitute an ultra-high-pressure metrology system centered on CCPGs, with sensors and pressure gauges serving as application-oriented measurement devices.

As CCPGs are developed toward higher pressures and lower uncertainties, they remain limited by factors such as the material strength of the PCA, pressure-dependent correction of the effective area, jacket-pressure control, sealing reliability, and high-pressure viscosity changes in pressure-transmitting media. In recent years, studies on finite-element analysis, fluid-dynamic modeling, sealing-structure optimization, and calibration-process automation have promoted the development of CCPGs toward multi-factor coupled correction.

For dynamic ultra-high-pressure metrology, drop-weight-based primary standards currently provide an established route for generating and calibrating high-amplitude transient liquid-pressure pulses. Diaphragmless shock tubes can generate rapid pressure steps, but their demonstrated metrological pressure range remains mainly in the MPa to several-tens-of-MPa range. With further advances in fast-valve technology, shock focusing, waveform characterization, and uncertainty evaluation, diaphragmless shock tubes

are expected to become an important method for ultra-high-pressure dynamic-pressure measurement and calibration.

Ultra-high-pressure secondary pressure standards play an important role in engineering field pressure measurement. Piezoresistive sensors have achieved GPa-level range extension through high-strength elastic bodies, SOI piezoresistive chips, and pressure-conversion structures. Resonant sensors have improved resolution and stability through frequency output, differential configurations, and temperature compensation. Emerging pressure-sensitive approaches, such as fiber-optic sensors and triboelectric sensors, further expand measurement possibilities in complex environments.

Extreme-pressure metrology has developed into a measurement landscape in which multiple methods, including ruby fluorescence, Raman spectroscopy, X-ray diffraction, and equations of state, are used in parallel. These methods have significantly extended the pressure-measurement range; however, most of them rely on reference materials, empirical calibration relationships, and equation-of-state models, and their traceability chains to the SI unit of pressure remain incomplete. The phase-transition points of Bi can serve as discrete reference anchors in the low-GPa range for connecting CCPGs with DAC experiments, but they cannot independently constitute a continuous traceability chain covering higher pressure ranges. Quantum sensing methods represented by NV centers provide a new theoretical direction for quantum-based traceability in extreme-pressure metrology, but they are still at the exploratory stage. Achieving accurate traceability of extreme-pressure measurements to pressure standards remains a central challenge in this field.

For CCPG-based ultra-high-pressure metrology, the uncertainty of the realized reference pressure can be propagated through the calibration model to gauges and sensors, together with contributions from sensor sensitivity, nonlinearity, temperature effects, repeatability, and other relevant characteristics. In contrast, although an uncertainty budget can be established for a specified DAC pressure scale and experimental condition, a single SI-traceable uncertainty budget cannot presently be propagated continuously from CCPG realization to extreme-pressure measurements. The discontinuity arises because the connection between the two regimes relies on discrete reference anchors and pressure-scale models, while subsequent DAC pressure determination is additionally affected by EOS assumptions and local experimental conditions, including non-hydrostatic stress, pressure gradients, temperature variation, and loading history. Establishing validated links across these stages is therefore essential before a continuous full-range uncertainty-propagation framework can be realized.

Author Contributions: Conceptualization, Q.T. and G.P.; methodology, Q.T. and Z.M.; investigation, Z.M.; resources, G.P. and Y.Y.; data curation, Z.M. and Y.W.; formal analysis, Z.M. and Y.W.; validation, Q.T., Y.L., G.P., and Y.Y.; writing—original draft preparation, Z.M. and Y.W.; writing—review and editing, Z.M., Y.W., Q.T., Y.L., G.P., and Y.Y.; visualization, Y.W. and Y.L.; supervision, Q.T., G.P., and Y.Y.; project administration, G.P.; funding acquisition, G.P. All authors have read and agreed to the published version of the manuscript.

Funding: This study received financial support from the National Key R&D Program of China under grant number 2024YFD2101102 (within program 2024YFD2101100). The APC was funded by the National Key Research and Development Program of China, grant number 2024YFD2101102.

Data Availability Statement: No new data were created or analyzed in this study. Data sharing is not applicable to this article.

Acknowledgments: The authors would like to acknowledge the assistance and support provided by the National Institute of Metrology, China.

Conflicts of Interest: The authors declare no conflicts of interest.

Abbreviations

The following abbreviations are used in this manuscript:

AIRAPT	Association for the Advancement of High Pressure Science and Technology
CCPG	controlled-clearance piston gauge
DAC	diamond anvil cell
DHS	di(2-ethylhexyl) sebacate
FS	full scale
GPa	gigapascal
IPPS	International Practical Pressure Scale
LNE	Laboratoire National de Métrologie et d'Essais
MEMS	micro-electro-mechanical systems
METAS	Federal Institute of Metrology
MPa	megapascal
NEMS	nanoelectromechanical systems
NIM	National Institute of Metrology, China
NRLM	National Research Laboratory of Metrology, Japan
NV	nitrogen-vacancy
ODMR	optically detected magnetic resonance
PCA	piston–cylinder assembly
PES-1	polyethylsiloxane
PTB	Physikalisch-Technische Bundesanstalt
SI	International System of Units
SIMT	Shanghai Institute of Measurement and Testing Technology
SOI	silicon-on-insulator
XRD	X-ray diffraction
π-FBG	π-phase-shifted fiber Bragg grating
GUM	Guide to the Expression of Uncertainty in Measurement

References

1. Zhang, S.; Liu, Q.; Liu, J.; Guo, J.; Li, R. A Cylindrical High-Temperature-Resistant Fiber-Optic Composite Sensor for Temperature and Pressure Measurement. *Sensors* **2026**, *26*, 417. [CrossRef]
2. Verma, J.; Ameli, N.; Kumar Katiyar, N.; Khatri, N.; Alsayegh, R.; Goel, S. Recent advances in ultra-precision manufacturing of electronic, photonic and quantum devices. *npj Adv. Manuf.* **2026**, *3*, 13. [CrossRef]
3. Farooq, S.A.; Iftikhar, S.H.; Albinmousa, J. A comprehensive review of hydrogen storage pressure vessels: Materials, fabrication, performance, testing procedures, and modelling approaches. *Int. J. Hydrogen Energy* **2026**, *224*, 154376. [CrossRef]
4. Hu, J.; Lv, C.; Deng, A.; Sun, P.; Liu, J.; Tian, Y. Saturated decomposition of calcium carbonate at high pressure and implication for deep carbon cycle. *Innov. Geosci.* **2026**, *4*, 100201. [CrossRef]
5. Mo, W.; Wang, X.; Zhang, L.; Zhang, Y.; Pan, X.; Xiao, K.; Chen, X.; Wang, L. Novel States of Matter in Quantum Materials Under High Pressure. *Adv. Quantum Technol.* **2026**, *9*, e00001. [CrossRef]
6. Han, X.; Sun, Y.; Huangfu, B.; He, X.; Huang, K. Ultra-high-pressure passivation of soybean agglutinin and safety evaluations. *Food Chem. X* **2023**, *18*, 100726. [CrossRef]
7. Shi, X.; Xie, H.; Li, C.; Li, J.; Liu, G.; You, Z.; Gao, M. Performance of a deep in situ pressure-preserving coring controller in a high-temperature and ultrahigh-pressure test system. *J. Rock Mech. Geotech. Eng.* **2025**, *17*, 877–896. [CrossRef]
8. Falgoust, M.; Kroll, P. Spinel-type Al_4C_3 attainable above 7 GPa and more high-pressure phases of Al_4C_3. *Chem. Sci.* **2026**, *17*, 2767–2771. [CrossRef]
9. Motaln, K.; Uran, E.; Giordano, N.; Parsons, S.; Lozinšek, M. Hydrostatic behaviour of highly inert Fomblin and Halocarbon fluids as pressure-transmitting media in high-pressure experiments. *Appl. Crystallogr.* **2025**, *58*, 221–226. [CrossRef]
10. Virant, M.; Lozinšek, M. CrimsonCalc: A software tool for pressure determination based on ruby fluorescence spectra. *Appl. Crystallogr.* **2025**, *58*, 1827–1833. [CrossRef]
11. Zhang, L.; Lu, J.; Li, H.; Li, B. Experimental study on the performance of concrete linear cutting by high pressure water jet. *Sci. Rep.* **2025**, *15*, 23144. [CrossRef]
12. Aghayar, Y.; Shahriari, A.; Moazzen, P.; Mohammadi, M. Hot Isostatic Pressing of Additively Manufactured Metallic Components: A Critical Review on Microstructure, Mechanical, and Corrosion Properties. *J. Mater. Res. Technol.* **2026**, *40*, 3343–3381. [CrossRef]

13. Sang, X.; Zhen, F.; Lv, P.; Zhang, Z.; Qu, B.; Wang, Y. Green and chemical-free pretreatment of flavonoids in tea plant seed husk using ultrasound-cold isostatic pressure synergistic extraction. *Food Chem.* **2025**, *478*, 143725. [CrossRef]
14. Chu, B.-S.; Lemos, M.A.; Blidi, S.; Kostic, B.; Di Monaco, R.; Miele, N.A.; Torrieri, E.; Ledbetter, M.; Rodríguez, Ó.; Fiore, A. Characterisation of fresh-like orange juice prepared by ultrasound treatment followed by high-pressure processing under industrial setting. *LWT* **2025**, *228*, 118019. [CrossRef]
15. Sánchez-Ordóñez, M.; Saraiva, J.A.; Pinto, C.A.; Delgado-Adámez, J.; Ramírez-Bernabé, M.R. Integral Valorisation of Agri-Food By-Products Through the Production of Food Ingredients Using High-Pressure Thermal Treatments. *Foods* **2025**, *14*, 2214. [CrossRef]
16. Hussain, N.; Qayyum, F.; Pasha, R.A.; Shah, M. Development of multi-physics numerical simulation model to investigate thermo-mechanical fatigue crack propagation in an autofrettaged gun barrel. *Def. Technol.* **2021**, *17*, 1579–1591. [CrossRef]
17. Zohrevand, M.; Rezaei, A.R.; Sabour, M.R.; Taherkhani, E.; Faraji, G. Recent progress on SPD processes empowered by hydrostatic pressure. *Mater. Trans.* **2023**, *64*, 1663–1672. [CrossRef]
18. Skiba, J.; Pachla, W.; Mazur, A.; Przybysz, S.; Kulczyk, M.; Przybysz, M.; Wróblewska, M. Press for hydrostatic extrusion with back-pressure and the properties of thus extruded materials. *J. Mater. Process. Technol.* **2014**, *214*, 67–74. [CrossRef]
19. Vogler, T.; Lee, M.; Grady, D. Static and dynamic compaction of ceramic powders. *Int. J. Solids Struct.* **2007**, *44*, 636–658. [CrossRef]
20. Campbell, L.; Menegon, L.; Fagereng, Å.; Pennacchioni, G. Earthquake nucleation in the lower crust by local stress amplification. *Nat. Commun.* **2020**, *11*, 1322. [CrossRef]
21. Alekseyev, N.I.; Broyko, A.P.; Khmelnitskiy, I.K.; Kolyadin, A.V.; Aivazyan, V.M.; Oreshko, I.V. Temperature-and Pressure-Reducing Regimes in the Growth Cell of HPHT Diamonds, Optimal for Preserving Crystal Integrity after Growth Completion. *C* **2023**, *9*, 52. [CrossRef]
22. Yang, L.; Lau, K.C.; Zeng, Z.; Zhang, D.; Tang, H.; Yan, B.; Niu, G.; Gou, H.; Yang, Y.; Yang, W. Synthesis of bulk hexagonal diamond. *Nature* **2025**, *644*, 370–375. [CrossRef]
23. Zhang, G.; Zhao, Y.; Zhao, Y.; Wang, X.; Wei, X.; Ren, W.; Li, H.; Zhao, Y. A manganin thin film ultra-high pressure sensor for microscale detonation pressure measurement. *Sensors* **2018**, *18*, 736. [CrossRef]
24. Zhang, R.; Chen, K.; Zhang, S.; Li, J.; Wei, S.; Yang, X. Anisotropy modulation and band structure reconstruction induced by high pressure in Kagome metal GdV6Sn6. *Superconductivity* **2025**, *15*, 100174. [CrossRef]
25. Duffy, T.S.; Smith, R.F. Ultra-high pressure dynamic compression of geological materials. *Front. Earth Sci.* **2019**, *7*, 23. [CrossRef]
26. Belonoshko, A.B.; Fu, J.; Bryk, T.; Simak, S.I.; Mattesini, M. Low viscosity of the Earth's inner core. *Nat. Commun.* **2019**, *10*, 2483. [CrossRef]
27. Ikuta, D.; Ohtani, E.; Fukui, H.; Sakai, T.; Ishikawa, D.; Baron, A.Q. Sound velocity of hexagonal close-packed iron to the Earth's inner core pressure. *Nat. Commun.* **2022**, *13*, 7211. [CrossRef]
28. Tian, Y.; Su, Z.; Chen, L.; Bu, Y.; Wang, H. Optimizing beveled diamond anvils via finite element analysis. *Int. J. Mech. Sci.* **2025**, *302*, 110602. [CrossRef]
29. Hilberer, A.; Loubeyre, P.; Pépin, C.; Occelli, F.; Weck, G.; André, R.; Dumas, P. Spectroscopic limits of diamond anvils to 520 GPa and projected bandgap closure. *Nat. Commun.* **2026**, *17*, 2644. [CrossRef]
30. Wisniewski, R.; Molinar, G. Pressure standards and sensors up to 3 GPa, actual state and development trends. *Phys. B Condens. Matter* **1999**, *265*, 246–253. [CrossRef]
31. Egan, P.F.; Stanfield, E.S.; Stoup, J.R.; Meyer, C.W. Conversion of a piston–cylinder dimensional dataset to the effective area of a mechanical pressure generator. *Metrologia* **2024**, *61*, 065004. [CrossRef]
32. Gavrilkin, S.; Borovkov, V.; Aslanyan, A.; Temnitskii, I.; Fedorov, A.; Yurov, L.; Aslanyan, E.; Shvydun, V.; Shchipunov, A. GET 43-2022 State Primary Standard for the unit of excess pressure within the static pressure range of 10–1600 MPa and the pulse pressure range of 1–1200 MPa and the effective area of piston-cylinder assemblies in deadweight testers within the range of 0.05–1 cm^2. *Meas. Tech.* **2023**, *66*, 637–646. [CrossRef]
33. Otal, P.; Yardin, C. Modelling methods for pressure balance calibration. *Meas. Sci. Technol.* **2020**, *31*, 034004. [CrossRef]
34. Sabuga, W.; Molinar, G.; Buonanno, G.; Esward, T.; Legras, J.; Yagmur, L. Finite element method used for calculation of the distortion coefficient and associated uncertainty of a PTB 1 GPa pressure balance—EUROMET project 463. *Metrologia* **2006**, *43*, 311–325. [CrossRef]
35. Dogra, S.; Yadav, S.; Bandyopadhyay, A. Computer simulation of a 1.0 GPa piston–cylinder assembly using finite element analysis (FEA). *Measurement* **2010**, *43*, 1345–1354. [CrossRef]
36. He, S.; Peng, Y.; Qiu, S.; Du, X.; Jin, Y. Sealing performance of sealing structure in a sediment sampler under ultra-high pressure. *Sci. Rep.* **2023**, *13*, 18548. [CrossRef]
37. Li, K.; Wang, Y.; Li, G.; Xu, Z.; Liu, Y.; Shi, A.; Yu, X.; Li, F. Optical Fiber Pressure Sensor with Self-Temperature Compensation Structure Based on MEMS for High Temperature and High Pressure Environment. *Photonics* **2025**, *12*, 258. [CrossRef]
38. Liu, M.; Wang, Z.; Jiang, P.; Yan, G. Temperature compensation method for piezoresistive pressure sensors based on gated recurrent unit. *Sensors* **2024**, *24*, 5394. [CrossRef]

39. Basov, M. Research of long-term stability of high-sensitivity piezoresistive pressure sensors for ultralow differential pressures. *IEEE Sens. J.* **2024**, *24*, 36443–36450. [CrossRef]
40. Hamid, Y.; Hutt, D.A.; Whalley, D.C.; Craddock, R. Relative contributions of packaging elements to the thermal hysteresis of a MEMS pressure sensor. *Sensors* **2020**, *20*, 1727. [CrossRef]
41. Fang, X.; Wu, C.; Tian, B.; Zhao, L.; Wei, X.; Jiang, Z. Pressure sensors based on the third-generation semiconductor silicon carbide: A comprehensive review. *Engineering* **2025**, *52*, 183–203. [CrossRef]
42. Zhang, Y.; Jiang, Y.; Deng, H.; Gao, H.; Tang, C.; Wang, X. All-sapphire-based optical fiber pressure sensor with an ultra-wide pressure range based on femtosecond laser micromachining and direct bonding. *Opt. Express* **2023**, *31*, 41967–41978. [CrossRef]
43. Salminen, J.; Högström, R.; Saxholm, S.; Lakka, A.; Riski, K.; Heinonen, M. Development of a primary standard for dynamic pressure based on drop weight method covering a range of 10 MPa–400 MPa. *Metrologia* **2018**, *55*, S52–S59. [CrossRef]
44. Sakai, T.; Kadobayashi, H.; Nakamoto, Y.; Dekura, H.; Ishimatsu, N.; Kawaguchi-Imada, S.; Seto, Y.; Sekizawa, O.; Nitta, K.; Shimizu, K. The equations of state of nine materials up to 0.43 TPa for extreme pressure science. *Commun. Mater.* **2025**, *6*, 68. [CrossRef]
45. Pease, A.; Zurkowski, C.; Chariton, S.; Krauss, H.N.; Sneed, D.; Prakapenka, V.; Baer, B.; Dorfman, S.M.; O'Bannon, E.F. Raman scattering of rhenium for secondary pressure calibration. *J. Appl. Phys.* **2025**, *137*, 195901. [CrossRef]
46. Ikoma, Y.; Sato, Y.; Kadobayashi, H.; Kawaguchi-Imada, S.; Han, S.Z.; Choi, E.; Arai, Y. High-pressure phase transformation and metastable phases of a Si0. 29Ge0. 71 alloy using a diamond anvil cell. *Appl. Phys. Lett.* **2025**, *127*, 071901.
47. Campbell, D.J.; Sneed, D.T.; O'Bannon, E.F., III; Söderlind, P.; Jenei, Z. Refined room-temperature equation of state of Bi up to 260 GPa. *Phys. Rev. B* **2023**, *107*, 224104. [CrossRef]
48. Liu, L.; Bi, Y. How far away are accurate equations of state determinations? Some issues on pressure scales and non-hydrostaticity in diamond anvil cells. *Matter Radiat. Extrem.* **2016**, *1*, 224–236. [CrossRef]
49. Chen, J.; Cheng, H.; Zhou, X.; Yan, X.; Wang, L.; Zhao, Y.; Wang, S. Calibration of manganin pressure gauge for diamond-anvil cells. *Rev. Sci. Instrum.* **2021**, *92*, 033905. [CrossRef]
50. Walker, D.; Li, J. Castable solid pressure media for multianvil devices. *Matter Radiat. Extrem.* **2020**, *5*, 018402. [CrossRef]
51. Decker, D.L.; Bassett, W.; Merrill, L.; Hall, H.; Barnett, J. High-pressure calibration: A critical review. *J. Phys. Chem. Ref. Data* **1972**, *1*, 773–836. [CrossRef]
52. Rab, S.; Yadav, S.; Haleem, A. A laconic capitulation of high pressure metrology. *Measurement* **2022**, *187*, 110226. [CrossRef]
53. Wen, P.; Wang, S.; Li, J.; Dong, K.; Ren, Z.; Li, Y.; Qu, R.; Li, T. Multiobjective optimization of a pressure maintaining ball valve structure based on RSM and NSGA-II. *Sci. Rep.* **2025**, *15*, 21342. [CrossRef] [PubMed]
54. Long, Y.; Li, S.; Liu, G.; Shen, L.; Liao, Z.; Lv, Y.; Zhong, Y.; Li, Y. Effects of hydraulic oil viscosity on the operational performance of ultra-high-pressure hydrogen diaphragm compressors. *Energy* **2025**, *330*, 136955. [CrossRef]
55. Jia, Z.; Wang, P.; Wei, J.; Zou, G.; Zhu, J.; Wang, J.; Guo, C. Research on the Metal Sealing Performance of a Casing Head Hanger Under High-Pressure Conditions. *Lubricants* **2026**, *14*, 43. [CrossRef]
56. Yang, C.; Hui, H.; Huang, S. Theoretical and experimental study on sealing performance of a novel ultra-high pressure bursting disc. *Proc. Inst. Mech. Eng. Part E J. Process Mech. Eng.* **2021**, *235*, 292–298. [CrossRef]
57. Huang, W.; Xie, H.; Li, J.; Yang, Y.; Li, C.; He, Z.; Li, Y.; Zhang, Z. Development of an In-Situ Simulation Device for Testing Deep Pressure-Preserving Coring Tools under High-Temperature and Ultrahigh-Pressure Conditions. *Appl. Sci.* **2023**, *13*, 3889. [CrossRef]
58. Che, J.; Chen, Z.; He, L.; Liao, J.; Zhang, Y. Micron-scale clearance high-pressure deformation and leakage flow characteristics in line seal plunger pair. *Phys. Fluids* **2025**, *37*, 052101. [CrossRef]
59. Samaan, N.D.; Abdullah, F. Characterisation of a 1 GPa piston-cylinder unit. *Measurement* **1998**, *23*, 179–183. [CrossRef]
60. Sharma, J.; Bandyopadhyay, A. Effect of viscosity of the pressure-transmitting fluid on the metrological characterization of the piston gauge up to 1 GPa. *Pramana* **1991**, *37*, 363–371. [CrossRef]
61. Xu, M.; Li, Y.; Ma, Y. Materials by design at high pressures. *Chem. Sci.* **2022**, *13*, 329–344. [CrossRef]
62. Sabuga, W.; Konczak, T.; Lorenz, F. Realisation of the liquid pressure scale from 0.5 MPa to 1.6 GPa at PTB. *Meas. Sens.* **2025**, *38*, 101680. [CrossRef]
63. Wilson, C.J.; Alvares, C.M.; Herlihy, A.; Funnell, N.P.; Sosso, G.C.; Senn, M.S. Optimal ratio or historical convention: The use of methanol–ethanol mixtures as pressure-transmitting mediums. *Appl. Crystallogr.* **2025**, *58*, 1967–1977. [CrossRef]
64. Chen, X.; Lou, H.; Zeng, Z.; Cheng, B.; Zhang, X.; Liu, Y.; Xu, D.; Yang, K.; Zeng, Q. Structural transitions of 4: 1 methanol–ethanol mixture and silicone oil under high pressure. *Matter Radiat. Extrem.* **2021**, *6*, 038402. [CrossRef]
65. Grocholski, B.; Jeanloz, R. High-pressure and-temperature viscosity measurements of methanol and 4: 1 methanol: Ethanol solution. *J. Chem. Phys.* **2005**, *123*, 204503.
66. Klotz, S.; Chervin, J.; Munsch, P.; Le Marchand, G. Hydrostatic limits of 11 pressure transmitting media. *J. Phys. D Appl. Phys.* **2009**, *42*, 075413. [CrossRef]

67. Chen, C.-C.; Appleton, R.J.; Mishra, S.; Nykiel, K.; Strachan, A. Discovery of new high-pressure phases–integrating high-throughput DFT simulations, graph neural networks, and active learning. *npj Comput. Mater.* **2025**, *11*, 191. [CrossRef]
68. Pope, A.D.; Xie, B.; Sereika, R.; Yang, W.; Chen, W.; Chen, H.; Cao, P.; Vohra, Y.K. Pressure induced irreversible phase transformation in an ordered high-entropy alloy. *Sci. Rep.* **2025**, *15*, 23227. [CrossRef]
69. Zhang, D.; Mandal, S.; Chung, D.Y.; Xu, J.; Shan, N.; Kanatzidis, M.G.; Chen, M. Pressure induced structural and electronic band transition in CsPbBr3. *Commun. Chem.* **2024**, *7*, 175. [CrossRef]
70. Liu, T.; Huang, Y.; Wang, S.; Wang, Y.; Cheng, P.; Wu, J. Phase transition, structural stability and electrical properties of V or Mn doped ZnSe composites under high pressure. *Sci. Rep.* **2025**, *15*, 5227. [CrossRef]
71. Hashad, A.S.; Ehlers, S.; Jusko, O.; Sabuga, W. Characterization of a force-balanced piston gauge as a primary pressure standard. *Measurement* **2019**, *131*, 723–729. [CrossRef]
72. Olson, D.A.; Driver, R.G.; Bowers, W.J. A gas pressure scale based on primary standard piston gauges. *J. Res. Natl. Inst. Stand. Technol.* **2010**, *115*, 393. [CrossRef]
73. Amer, E.; Jönsson, G.; Arrhén, F. Secondary measurement standard for calibration of dynamic pressure sensor to bridge the gap between existing static and dynamic standards. *Measurement* **2025**, *242*, 116253. [CrossRef]
74. Singh, J.; Kumaraswamidhas, L.A.; Bura, N.; Rab, S.; Sharma, N.D. Characterization of a standard pneumatic piston gauge using finite element simulation technique vs cross-float, theoretical and Monte Carlo approaches. *Adv. Eng. Softw.* **2020**, *150*, 102920. [CrossRef]
75. Forman, R.A.; Piermarini, G.J.; Barnett, J.D.; Block, S. Pressure measurement made by the utilization of ruby sharp-line luminescence. *Science* **1972**, *176*, 284–285. [CrossRef]
76. Johnson, D.; Heydemann, P. Dead Weight Piston Gauge for Pressures to 26 Kilobars. *Rev. Sci. Instrum.* **1967**, *38*, 1294–1300. [CrossRef]
77. Zheng, Z.; Song, Y.; Zheng, B.; Zhao, Y.; Wang, Q.; Zhang, X.; Zou, B.; Zou, H. Eu^{2+} and Mn^{2+} co-doped $Lu_2Mg_2Al_2Si_2O_{12}$ phosphors for high sensitivity and multi-mode optical pressure sensing. *Inorg. Chem. Front.* **2023**, *10*, 2788–2798. [CrossRef]
78. Wang, X.; Chen, T.; Qi, X.; Zou, Y.; Kung, J.; Yu, T.; Wang, Y.; Liebermann, R.C.; Li, B. Acoustic travel time gauges for in-situ determination of pressure and temperature in multi-anvil apparatus. *J. Appl. Phys.* **2015**, *118*, 065901. [CrossRef]
79. Barnett, J.; Block, S.; Piermarini, G. An optical fluorescence system for quantitative pressure measurement in the diamond-anvil cell. *Rev. Sci. Instrum.* **1973**, *44*, 1–9. [CrossRef]
80. Shen, G.; Smith, J.S.; Kenney-Benson, C.; Wang, Y. Calibration of ruby's luminescence shift from the bismuth I-II transition: Constraints on the initial slope of ruby gauge. *High Press. Res.* **2025**, *45*, 17–28. [CrossRef]
81. Getting, I. New determination of the bismuth I-II equilibrium pressure: A proposed modification to the practical pressure scale. *Metrologia* **1998**, *35*, 119–132. [CrossRef]
82. *JCGM 100:2008*; Evaluation of Measurement Data—Guide to the Expression of Uncertainty in Measurement. Joint Committee for Guides in Metrology: Sèvres, France, 2008.
83. Fei, Y.; Ricolleau, A.; Frank, M.; Mibe, K.; Shen, G.; Prakapenka, V. Toward an internally consistent pressure scale. *Proc. Natl. Acad. Sci. USA* **2007**, *104*, 9182–9186. [CrossRef]
84. Paudel, H.P.; Lander, G.R.; Crawford, S.E.; Duan, Y. Sensing at the nanoscale using nitrogen-vacancy centers in diamond: A model for a quantum pressure sensor. *Nanomaterials* **2024**, *14*, 675. [CrossRef]
85. Shen, G.; Wang, Y.; Dewaele, A.; Wu, C.; Fratanduono, D.E.; Eggert, J.; Klotz, S.; Dziubek, K.F.; Loubeyre, P.; Fat'yanov, O.V. Toward an international practical pressure scale: A proposal for an IPPS ruby gauge (IPPS-Ruby2020). *High Press. Res.* **2020**, *40*, 299–314. [CrossRef]
86. Cook, R.F.; Michaels, C.A. Coefficients for stress, temperature, and composition effects in fluorescence measurements of alumina. *J. Res. Natl. Inst. Stand. Technol.* **2017**, *122*, 43. [CrossRef]
87. Sims, M.; Jaret, S.J.; Johnson, J.R.; Whitaker, M.L.; Glotch, T.D. Unconventional high-pressure Raman spectroscopy study of kinetic and peak pressure effects in plagioclase feldspars. *Phys. Chem. Miner.* **2020**, *47*, 12. [CrossRef]
88. Torikachvili, M.; Kim, S.; Colombier, E.; Bud'Ko, S.; Canfield, P. Solidification and loss of hydrostaticity in liquid media used for pressure measurements. *Rev. Sci. Instrum.* **2015**, *86*, 123904. [CrossRef]
89. Liu, C.; Wang, C.; Zhang, Z.; Lin, Z.; Feng, M. Characteristic analysis of a controlled-clearance piston-cylinder assembly up to 1500 MPa using a finite element method. *Metrologia* **2023**, *60*, 065007. [CrossRef]
90. Sabuga, W.; Rabault, T.; Wüthrich, C.; Pražák, D.; Chytil, M.; Brouwer, L.; Ahmed, A.D. High pressure metrology for industrial applications. *Metrologia* **2017**, *54*, S108–S124. [CrossRef]
91. Yue, J.; Gluschko, A.; Sabuga, W. Characterization of the new 1 GPa piston-cylinder assembly of PTB. *Measurement* **2019**, *134*, 788–793. [CrossRef]
92. Samodro, R.A.; Choi, I.-M.; Woo, S.-Y. Investigation of 1 GPa Controlled Clearance Piston Gauge Using Finite Element Analysis: RA Samodro et al. *MAPAN* **2020**, *35*, 105–110.

93. Bakhvalova, V.; Zolotykh, E.; Borovkov, V. State special standard for pressure units in the range from $2500 \cdot 10^5$ to $15000 \cdot 10^5$ Pa. *Meas. Tech.* **1973**, *16*, 1603–1605. [CrossRef]
94. Eremeev, A. Reference free-piston manometer measuring to 2.6 GPa. *Meas. Tech.* **1974**, *17*, 1004–1007. [CrossRef]
95. Peggs, G.; Lewis, S. The NPL primary pressure balance standard. *J. Phys. E Sci. Instrum.* **1977**, *10*, 1028–1034. [CrossRef]
96. Sharma, J.; Jain, K. Accurate measurement of pressure. *Pramana* **1986**, *27*, 417–434. [CrossRef]
97. Legras, J. Pressure balance used as standard in the pressure range 0.1 to 1 Gpa. *High Press. Res.* **1991**, *7*, 82–84. [CrossRef]
98. Molinar, G. An old instrument in the new technological scenery: The piston gauge in liquid media up to 1 GPa. *Metrologia* **1994**, *30*, 615–623. [CrossRef]
99. Bandyopadhyay, A.K.; Olson, D.A. Characterization of a compact 200 MPa controlled clearance piston gauge as a primary pressure standard using the Heydemann and Welch method. *Metrologia* **2006**, *43*, 573–582. [CrossRef]
100. Kajikawa, H.; Kobata, T.; Ooiwa, A. Development of a new controlled-clearance pressure balance for hydraulic high-pressure standard. In *Proceedings of the SICE Annual Conference 2007, Takamatsu, Japan, 17–20 September 2007*; IEEE: New York, NY, USA, 2007; pp. 384–387.
101. Borovkov, V.; Kuznetsov, D.; Sekoyan, S.; Shchipunov, A.; Aslanyan, A.; Gavrilkin, S. Creation of a National Primary Standard for the Unit of Pressure in the Range of 10–1600 MPa. *Meas. Tech.* **2015**, *57*, 1233–1237. [CrossRef]
102. Hong, B.; Pan, Z.; Gu, S.; Zhang, Z. An Investigation of the High Pressure Controlled Clearance Dead Weight Piston Gauge. In *Proceedings of the 2018 5th International Conference on Systems and Informatics (ICSAI), Nanjing, China, 10–12 November 2018*; IEEE: New York, NY, USA, 2018; pp. 734–738.
103. Johnson, D.; Newhall, D. The piston gage as a precise pressure-measuring instrument. *Trans. Am. Soc. Mech. Eng.* **1953**, *75*, 301–310. [CrossRef]
104. Nishibata, K.; Yamamoto, S.; Kaneda, R. A dead-weight piston manometer for use up to 2 GPa. *Jpn. J. Appl. Phys.* **1980**, *19*, 2245. [CrossRef]
105. Gu, S.J.; Wang, L.; Liu, J.X.; Dai, X.H.; Pan, Z.Y.; Pan, D.Z. A Study of Controlled-Clearance Deadweight Piston Gauge for Pressure up to 1500 MPa. *Acta Metrol. Sin.* **2008**, *29*, 54–59.
106. Sabuga, W.; Haines, R. Development of 1.6 GPa pressure-measuring multipliers. *Acta IMEKO* **2014**, *3*, 54–59. [CrossRef]
107. Sanjid, M.A.; Chaudhary, K.; Yadav, S.; Sen, M.; Ghoshal, S.K. A novel method of diameter measurement of pistons used in pressure standards using scanning principle and fusion technique. *Meas. Sci. Technol.* **2018**, *29*, 085008. [CrossRef]
108. Stoup, J.; Doiron, T. A novel high accuracy micrometer for the measurement of diameter. *Metrologia* **2021**, *58*, 025002. [CrossRef]
109. Sabuga, W.; Hashad, A.; Ehlers, S. 2D flow model for calculating effective area of piston-cylinder units. *Acta IMEKO* **2020**, *9*, 319–324. [CrossRef]
110. Aslanyan, A. Dependence of the characteristics of a high-pressure piston pair on the properties of pes-3 working fluid and the pressure distribution in the piston-cylinder gap. *Meas. Tech.* **2021**, *63*, 811–815. [CrossRef]
111. Liu, C.; Zhang, Z.; Hong, B.; Wang, C.; Lin, Z.; Feng, M.; Zhang, J. Elastic Distortion Calculation of a Controlled-Clearance Piston-Cylinder Assembly up to 1500 MPa Using Finite Element Method. *J. Phys. Conf. Ser.* **2022**, *2264*, 012013. [CrossRef]
112. Wongthep, P.; Sainoo, L. The calculation of pressure distorsion coefficient of pressure balance 500 MPA by using a finite element method. *Meas. Sens.* **2025**, *38*, 101683. [CrossRef]
113. Ginanjar, G.; Choi, I.-M. A study on the tilt effect of pressure balance up to 500 MPa. *Meas. Sens.* **2021**, *18*, 100342. [CrossRef]
114. Ginanjar, G.; Choi, I.-M.; Kim, S.-M. PCA exchange method for compensation of error sources in pressure balance calibration. *Measurement* **2018**, *124*, 179–183. [CrossRef]
115. Sharma, J.; Jain, K.K.; Bean, V.E.; Welch, B.; Lazos, R.J. Effects of viscosity, temperature, and rate of rotation on pressure generated by a controlled-clearance piston gauge. *Rev. Sci. Instrum.* **1984**, *55*, 563–569. [CrossRef]
116. Huang, W.; Feng, G.; He, H.-L.; Chen, J.-Z.; Wang, J.-Q.; Zhao, Z. Development of an ultra-high-pressure rotary combined dynamic seal and experimental study on its sealing performance in deep energy mining conditions. *Pet. Sci.* **2022**, *19*, 1305–1321. [CrossRef]
117. Han, T.; Fan, J. Measurement and evaluation of metal-to-metal seals sealability by ultrasonic phased array. *Metals* **2023**, *13*, 1032. [CrossRef]
118. Yang, Z.; Li, J.; Long, H.; Wang, N. Research on the influence of cone angle on the sealing performance of pipeline joint. *J. Phys. Conf. Ser.* **2024**, *2755*, 012006. [CrossRef]
119. Yadav, S.; Prakash, O.; Gupta, V.; Bandyopadhyay, A. The effect of pressure-transmitting fluids in the characterization of a controlled clearance piston gauge up to 1 GPa. *Metrologia* **2007**, *44*, 222–233. [CrossRef]
120. Scherschligt, J.; Cross, C.D.; Quintavalle, J.; Yang, Y.; Driver, R.G.; Schlatter, K.; Olson, D.A. Automated Piston Gauge Calibration System. *NCSLI Meas.* **2018**, *12*, 42–45. [CrossRef]
121. Liao, W.; Chen, Y.; Wang, N. Experimental Investigation on Pressure and Flame Surface Oscillation in a Dual-Cavity Scramjet Combustor. *Energies* **2024**, *17*, 1639. [CrossRef]

122. Yang, F.; Zhu, H.; Kong, D.; Zhao, C. Accurate Measurement of Blast Shock Wave Pressure by Enhanced Sensor System Based on Neural Network. *Sensors* **2025**, *25*, 6187. [CrossRef]
123. Zhao, Z.; Wu, Y. Standardizing the Ignition Delay Time Measurements of Rapid Compression Machine: An Inverse Application of the Livengood–Wu Integral Method. *Energies* **2025**, *18*, 165. [CrossRef]
124. Zhou, Z.; Li, H.; Chen, J.; Li, D.; Zhang, N. Numerical simulation on transient pressure pulsations and complex flow structures of a ultra-high-speed centrifugal pump at stalled condition. *Energies* **2023**, *16*, 4476. [CrossRef]
125. Pereira, J.D. Pressure sensors: Working principles of static and dynamic calibration. *Sensors* **2024**, *24*, 629. [CrossRef]
126. Sanchez, K.; Achour, B.; Coustou, A.; Lecestre, A.; Charlot, S.; Lavayssière, M.; Lefrançois, A.; Aubert, H.; Pons, P. Transient response of miniature piezoresistive pressure sensor dedicated to blast wave monitoring. *Sensors* **2022**, *22*, 9571. [CrossRef]
127. Svete, A.; Kutin, J. Characterization of a newly developed diaphragmless shock tube for the primary dynamic calibration of pressure meters. *Metrologia* **2020**, *57*, 055009. [CrossRef]
128. Amer, E.; Jönsson, G.; Arrhén, F. Towards traceable dynamic pressure calibration using a shock tube with an optical probe for accurate phase determination. *Metrologia* **2022**, *59*, 035001. [CrossRef]
129. Choi, I.-M.; Yang, I.; Woo, S.-Y. High dynamic pressure standard based on the density change of the step pressure generator. *Metrologia* **2013**, *50*, 631–636. [CrossRef]
130. Liu, D.; Liu, A.; Zhang, F.; Gang, X.; Li, L.; Wu, H. A dynamic pressure calibration device based on the low speed servomotor and pistonphone technique. *Measurement* **2020**, *151*, 107254. [CrossRef]
131. Svete, A.; Novak, B.; Planko, U.; Kutin, J. Experimental investigation of the developed focusing elements for generating extreme pressures in a diaphragmless shock tube. *Sci. Rep.* **2025**, *15*, 23929. [CrossRef]
132. Castro, F.J.H.; Kutin, J.; Svete, A. Effects of the opening speed of the valve in a diaphragmless shock tube for metrological purposes. *IEEE Sens. J.* **2023**, *24*, 158–168. [CrossRef]
133. Coombs, D.; Akih-Kumgeh, B. Numerical investigation of the impact of tailored driver gases and driver inserts on shock tube flows: D. Coombs, B. Akih-Kumgeh. *Shock Waves* **2018**, *28*, 1097–1107.
134. Novak, B.; Svete, A.; Kutin, J. Effects of the shock tube diameter on shock wave propagation in a diaphragmless shock tube. *Meas. Sens.* **2025**, *38*, 101687. [CrossRef]
135. Platte, T.; Iwanczik, M.; Mende, M. A new primary approach for dynamic and periodic pressure transducer calibration. In *Proceedings of the Sensors and Measuring Systems, 19th ITG/GMA-Symposium, Nuremberg, Germany, 26–27 June 2018*; VDE Verlag GmbH: Berlin/Offenbach, Germany, 2018; pp. 1–4.
136. Durgut, Y.; Ganioglu, O.; Aydemir, B.; Turk, A.; Yilmaz, R.; Hamarat, A.; Bagci, E. Improvement of dynamic pressure standard for calibration of dynamic pressure transducers. In *Proceedings of the 19th International Congress of Metrology (CIM2019), Paris, France, 24–26 September 2019*; EDP Sciences: Les Ulis, France, 2019; p. 27009.
137. Yang, F.; Kong, D.; Wang, F.; Kong, L. A traceable dynamic calibration research of the measurement system based on quasi-static and dynamic calibration for accurate blast overpressure measurement. *Meas. Sci. Technol.* **2019**, *30*, 025005. [CrossRef]
138. Mokhtar, A.H.; Rashad, R.M.; Osman, T.; Eltawil, A.A.; Gelany, S.A. Numerical Modeling and Analysis of the Pressure Pulse Generated by Drop Mass Calibration Device. *Instrum. Mes. Metrol.* **2024**, *23*, 193. [CrossRef]
139. Yılmaz, R.; Arıkan, H.; Durgut, Y.; Hamarat, A. Determination of parameters generating the reference pressure in the primary level dynamic pressure measurement system based on the drop weight method. *Metrol. Meas. Syst.* **2024**, *31*, 85–102. [CrossRef]
140. Högström, R.; Lakka, A.; Hämäläinen, J.; Salonen, L.; Brzozowski, A. Novel primary standard for dynamic pressure up to 500 MPa. *Meas. Sens.* **2025**, *38*, 101686. [CrossRef]
141. Yao, Z.; Li, Y.; Ding, Y.; Wang, C.; Yao, L.; Song, J. Improved shock tube method for dynamic calibration of the sensitivity characteristic of piezoresistive pressure sensors. *Measurement* **2022**, *196*, 111271. [CrossRef]
142. Amer, E.; Wozniak, M.; Jönsson, G.; Arrhén, F. Evaluation of shock tube retrofitted with fast-opening valve for dynamic pressure calibration. *Sensors* **2021**, *21*, 4470. [CrossRef]
143. Yao, Z.; Liu, X.; Wang, C.; Yang, W. Improved traceable measurement of the reflected step pressure in shock tube with the compensation of shock wave attenuation. *Aerosp. Sci. Technol.* **2020**, *107*, 106302. [CrossRef]
144. Shi, B.; Yao, Z.; Li, F.; Chen, X.; Yao, L.; Ding, Y. Identifying the frequency characteristics of the pressure measurement system with a pressure transmission tube using shock tube method. *Measurement* **2025**, *242*, 116293. [CrossRef]
145. Svete, A.; Kutin, J. Diaphragmless shock tube for primary dynamic calibration of pressure meters. *Acta IMEKO* **2020**, *9*, 310–314. [CrossRef]
146. Jousten, K. Traceability to SI units for vacuum measurement in industrial applications. *Measurement* **2012**, *45*, 2420–2425. [CrossRef]
147. Brunelli, R. *Template Matching Techniques in Computer Vision: Theory and Practice*; John Wiley & Sons: Hoboken, NJ, USA, 2009.
148. Abiodun, O.I.; Jantan, A.; Omolara, A.E.; Dada, K.V.; Umar, A.M.; Linus, O.U.; Arshad, H.; Kazaure, A.A.; Gana, U.; Kiru, M.U. Comprehensive review of artificial neural network applications to pattern recognition. *IEEE Access* **2019**, *7*, 158820–158846. [CrossRef]

149. Li, Y. Research and application of deep learning in image recognition. In *Proceedings of the 2022 IEEE 2nd International Conference on Power, Electronics and Computer Applications (ICPECA), Shenyang, China, 21–23 January 2022*; IEEE: New York, NY, USA, 2022; pp. 994–999.
150. Qin, R.; Hu, M.; Li, X.; Yan, L.; Wu, C.; Liu, J.; Gao, H.; Shan, G.; Huang, W. A highly sensitive piezoresistive sensor based on MXenes and polyvinyl butyral with a wide detection limit and low power consumption. *Nanoscale* **2020**, *12*, 17715–17724. [CrossRef]
151. Zhao, Y.; Fang, X.; Jiang, Z.; Zhao, L. An ultra-high pressure sensor based on SOI piezoresistive material. *J. Mech. Sci. Technol.* **2010**, *24*, 1655–1660. [CrossRef]
152. Zhang, G.-D.; Zhao, Y.-L.; Zhao, Y.; Wang, X.-C.; Wei, X.-Y. Research of a novel ultra-high pressure sensor with high-temperature resistance. *Micromachines* **2017**, *9*, 5. [CrossRef]
153. Sinha, A.; Priyadarshi, P.; Muralidharan, B. Ballistic graphene arrays for ultra-high pressure sensing. *J. Appl. Phys.* **2022**, *132*, 154501. [CrossRef]
154. Zhang, Q.; Li, C.; Zhao, Y.; Zhang, Z. A quartz resonant ultra-high pressure sensor with high precision and high stability. *IEEE Sens. J.* **2021**, *21*, 22553–22561. [CrossRef]
155. Zhang, Q.; Li, C.; Li, H.; Liu, Y.; Wang, J.; Wang, X.; Wang, Y.; Cheng, F.; Han, H.; Zhang, P. A high-precision quartz resonant ultra-high pressure sensor with integrated pressure conversion structure. *Micromachines* **2023**, *14*, 1657. [CrossRef]
156. Qian, P.; Yu, Z.; Yu, J.; Lu, Y.; Xie, B.; Chen, J.; Chen, D.; Wang, J. A resonant high-pressure microsensor based on a composite pressure-sensitive mechanism of diaphragm bending and volume compression. *Microsyst. Nanoeng.* **2024**, *10*, 38. [CrossRef]
157. Zhang, W.; Xu, Y.; Zhang, Z.; Jing, J.; Yao, B.; Gao, L.; Xue, C.; Tian, Z. Dual-mode AT-cut quartz resonant pressure sensor for wide pressure and temperature measurement ranges. *Sens. Actuators A Phys.* **2025**, *382*, 116103. [CrossRef]
158. Ye, P.; Yu, Z.; Tan, Z.; Xie, B.; Lu, Y.; Chen, D.; Wang, J. Extreme Environment-Compatible silicon resonant pressure sensors with high precision and reliability. *Measurement* **2025**, *256*, 118275. [CrossRef]
159. Qi, X.; Wang, S.; Jiang, J.; Liu, K.; Wang, X.; Yang, Y.; Liu, T. Fiber optic Fabry-Perot pressure sensor with embedded MEMS micro-cavity for ultra-high pressure detection. *J. Light. Technol.* **2019**, *37*, 2719–2725. [CrossRef]
160. Sun, Q.; Zhang, M.; Zhao, S.; Ji, L.; Su, J.; Xu, J.; Yang, B.; Wu, C. Performance and analysis of pressure sensor with π-FBG on thick-walled cylinder for ultra-high oceanic pressure measurement. *Opt. Lasers Eng.* **2025**, *194*, 109147. [CrossRef]
161. Hu, J.; Liu, Z.; Yang, P.; Qin, S.; Li, N.; Ji, W.; Wang, Z.L.; Chen, X. Charge transfer behavior of triboelectric polymers and triboelectric sensors operated under ultrahigh pressure. *SusMat* **2024**, *4*, e250. [CrossRef]
162. Zhou, Y.; Dong, Z.-Y.; Hsieh, W.-P.; Goncharov, A.F.; Chen, X.-J. Thermal conductivity of materials under pressure. *Nat. Rev. Phys.* **2022**, *4*, 319–335. [CrossRef]
163. Fuller, P.; Price, J. Dynamic pressure measurements to 300 kilobars with a resistance transducer. *Br. J. Appl. Phys.* **1964**, *15*, 751–758. [CrossRef]
164. Fratanduono, D.; Smith, R.; Ali, S.; Braun, D.; Fernandez-Pañella, A.; Zhang, S.; Kraus, R.; Coppari, F.; McNaney, J.; Marshall, M. Probing the solid phase of noble metal copper at terapascal conditions. *Phys. Rev. Lett.* **2020**, *124*, 015701. [CrossRef]
165. Wei, B.; Lin, L.; Zhang, J.; Zhan, Z.; Cheng, Z.; Jiang, J. In situ measurement techniques using diamond anvil cell at high pressure–temperature conditions: A review. *Phys. Status Solidi (RRL)–Rapid Res. Lett.* **2024**, *18*, 2300469. [CrossRef]
166. Dewaele, A.; Loubeyre, P.; Occelli, F.; Marie, O.; Mezouar, M. Toroidal diamond anvil cell for detailed measurements under extreme static pressures. *Nat. Commun.* **2018**, *9*, 2913. [CrossRef]
167. Dubrovinsky, L.; Dubrovinskaia, N.; Prakapenka, V.B.; Abakumov, A.M. Implementation of micro-ball nanodiamond anvils for high-pressure studies above 6 Mbar. *Nat. Commun.* **2012**, *3*, 1163. [CrossRef]
168. Wang, J.; Tian, Y.; Su, Y.; Xiang, X.; Zhou, L.; Huang, M.; Zhang, L.; He, D. Graphite/diamond transformation mechanism under the action of an iron-based catalyst. *CrystEngComm* **2023**, *25*, 1884–1893. [CrossRef]
169. Hirao, N.; Kawaguchi, S.; Hirose, K.; Shimizu, K.; Ohtani, E.; Ohishi, Y. New developments in high-pressure X-ray diffraction beamline for diamond anvil cell at SPring-8. *Matter Radiat. Extrem.* **2020**, *5*, 018403. [CrossRef]
170. Kono, Y.; Kenney-Benson, C.; Shen, G. Opposed type double stage cell for Mbar pressure experiment with large sample volume. *High Press. Res.* **2020**, *40*, 175–183. [CrossRef]
171. Kuwayama, Y.; Morard, G.; Nakajima, Y.; Hirose, K.; Baron, A.Q.; Kawaguchi, S.I.; Tsuchiya, T.; Ishikawa, D.; Hirao, N.; Ohishi, Y. Equation of state of liquid iron under extreme conditions. *Phys. Rev. Lett.* **2020**, *124*, 165701. [CrossRef]
172. Bean, V.; Akimoto, S.; Bell, P.; Block, S.; Holzapfel, W.; Manghnani, M.; Nicol, M.; Stishov, S. Another step toward an international practical pressure scale: 2nd AIRAPT IPPS task group report. *Phys. B+ C* **1986**, *139*, 52–54.
173. Ito, E. Report on the first international pressure calibration workshop. *Rev. High Press. Sci. Technol.* **1998**, *7*, 151–153. [CrossRef]
174. Funamori, N.; Jeanloz, R. High-pressure transformation of Al_2O_3. *Science* **1997**, *278*, 1109–1111. [CrossRef]
175. Ono, S.; Oganov, A.R.; Koyama, T.; Shimizu, H. Stability and compressibility of the high-pressure phases of Al2O3 up to 200 GPa: Implications for the electrical conductivity of the base of the lower mantle. *Earth Planet. Sci. Lett.* **2006**, *246*, 326–335. [CrossRef]

176. Eremets, M.; Minkov, V.S.; Kong, P.; Drozdov, A.; Chariton, S.; Prakapenka, V. Universal diamond edge Raman scale to 0.5 terapascal and implications for the metallization of hydrogen. *Nat. Commun.* **2023**, *14*, 907. [CrossRef]
177. Heinz, D.L. Thermal pressure in the laser-heated diamond anvil cell. *Geophys. Res. Lett.* **1990**, *17*, 1161–1164. [CrossRef]
178. Dewaele, A.; Fiquet, G.; Gillet, P. Temperature and pressure distribution in the laser-heated diamond–anvil cell. *Rev. Sci. Instrum.* **1998**, *69*, 2421–2426. [CrossRef]
179. Feng, B.; Zarechnyy, O.M.; Levitas, V.I. Strain-induced phase transformations under compression, unloading, and reloading in a diamond anvil cell. *J. Appl. Phys.* **2013**, *113*, 173514. [CrossRef]
180. Nayak, A.P.; Bhattacharyya, S.; Zhu, J.; Liu, J.; Wu, X.; Pandey, T.; Jin, C.; Singh, A.K.; Akinwande, D.; Lin, J.-F. Pressure-induced semiconducting to metallic transition in multilayered molybdenum disulphide. *Nat. Commun.* **2014**, *5*, 3731. [CrossRef]
181. Li, J.; Sturhahn, W.; Jackson, J.; Struzhkin, V.; Lin, J.; Zhao, J.; Mao, H.; Shen, G. Pressure effect on the electronic structure of iron in (Mg,Fe)(Si,Al)O_3 perovskite: A combined synchrotron Mössbauer and X-ray emission spectroscopy study up to 100 GPa. *Phys. Chem. Miner.* **2006**, *33*, 575–585. [CrossRef]
182. Ohishi, Y.; Hirao, N.; Sata, N.; Hirose, K.; Takata, M. Highly intense monochromatic X-ray diffraction facility for high-pressure research at SPring-8. *High Press. Res.* **2008**, *28*, 163–173. [CrossRef]
183. Goncharov, A.F. Raman spectroscopy at high pressures. *Int. J. Spectrosc.* **2012**, *2012*, 617528. [CrossRef]
184. Matsumura, T.; Kuwayama, Y.; Ueki, K.; Kuwatani, T.; Ando, Y.; Nagata, K.; Ito, S.-I.; Nagao, H. Bayesian modeling of the equation of state for liquid iron in Earth's outer core. *J. Geophys. Res. Solid Earth* **2021**, *126*, e2021JB023062. [CrossRef]
185. Potapkin, V.; Chumakov, A.I.; Smirnov, G.V.; Celse, J.-P.; Rüffer, R.; McCammon, C.; Dubrovinsky, L. The 57Fe synchrotron Mössbauer source at the ESRF. *Synchrotron Radiat.* **2012**, *19*, 559–569. [CrossRef]
186. Ono, S. High-pressure phase transition of bismuth. *High Press. Res.* **2018**, *38*, 414–421. [CrossRef]
187. Chen, H.-Y.; Xiang, S.-K.; Yan, X.-Z.; Zheng, L.-R.; Zhang, Y.; Liu, S.-G.; Bi, Y. Phase transition of solid bismuth under high pressure. *Chin. Phys. B* **2016**, *25*, 108103. [CrossRef]
188. Suda, R.; Uriu, K.; Yamamoto, K.; Sasaki, M.; Sasaki, K.; Einaga, M.; Shimizu, K.; Kobayashi, K. GPa pressure imaging using nanodiamond quantum sensors. *J. Phys. Soc. Jpn.* **2025**, *94*, 124707. [CrossRef]
189. Ho, K.O.; Leung, M.Y.; Wang, W.; Xie, J.; Yip, K.Y.; Wu, J.; Goh, S.K.; Denisenko, A.; Wrachtrup, J.; Yang, S. Spectroscopic study of N-V sensors in diamond-based high-pressure devices. *Phys. Rev. Appl.* **2023**, *19*, 044091. [CrossRef]
190. Acosta, V.M.; Bauch, E.; Ledbetter, M.P.; Waxman, A.; Bouchard, L.-S.; Budker, D. Temperature dependence of the nitrogen-vacancy magnetic resonance in diamond. *Phys. Rev. Lett.* **2010**, *104*, 070801. [CrossRef]
191. *JCGM 200:2012*; International Vocabulary of Metrology—Basic and General Concepts and Associated Terms (VIM), 3rd ed. Joint Committee for Guides in Metrology: Sèvres, France, 2012.
192. Jcgm, J. Evaluation of measurement data—Guide to the expression of uncertainty in measurement. *Int. Organ. Stand. Geneva* **2008**, *50*, 134.
193. Cui, J.; Zhang, S.; Jiang, Y. Design of a Rapid and Accurate Calibration System for Pressure Sensors with Minimized Temperature Variation. *Sensors* **2025**, *25*, 5288. [CrossRef]
194. Zhou, M.; Zhou, S.; Zhou, Z.; Jiang, S.; Zhang, W. Design, fabrication, and thermal zero drift compensation of a SOI pressure sensor for high temperature applications. *Sens. Actuators A Phys.* **2025**, *382*, 116151. [CrossRef]
195. Zhang, Y.; Liu, F.; Zhou, Z.; Liang, X.; Sun, R.; Deng, J.; Luo, X.; Lin, J.; Chen, X.; Zhang, X. Near-zero nonlinear error pressure sensor based on piezoresistor sensitivity matching for wind tunnel pressure test. *Microsyst. Nanoeng.* **2025**, *11*, 122. [CrossRef]
196. Wang, L.; Wan, N.; Yang, Y.; Wang, Y.; Zhao, Y.; Zhu, J.; Yang, M.; Lyu, Y.; Liu, M.; Zhao, Y. Development of leadless packaged heavily doped N-type 4H-SiC pressure sensor family for harsh environments. *Microsyst. Nanoeng.* **2025**, *11*, 74. [CrossRef]
197. Houck, J.C. Temperature coefficient of the bismuth I–II transition pressure. *J. Res. Natl. Bur. Stand. Sect. A Phys. Chem.* **1970**, *74*, 51. [CrossRef]
198. Vanfleet, H.; Zeto, R.J. Comparison of the Bismuth I–II Phase Transformations in Liquid and Solid High-Pressure Systems. *J. Appl. Phys.* **1971**, *42*, 4955–4960. [CrossRef]
199. Schaffrinna, T.; Schröck, C.; Milman, V.; Winkler, B. Pathways for martensitic high-pressure phase transitions in bismuth. *Phys. Rev. B* **2025**, *111*, 174111. [CrossRef]
200. Wang, Y.; Shen, G.; Leinenweber, K.; Dewaele, A.; Katsura, T.; Nishihara, Y.; Ishii, T.; Eggert, J.; Dziubek, K.; Force, A.I.T. PIPS-2025: An updated practical pressure scale for the large-volume presses. *High Press. Res.* **2026**, *46*, 1–21. [CrossRef]
201. Segawa, T.F.; Igarashi, R. Nanoscale quantum sensing with Nitrogen-Vacancy centers in nanodiamonds–A magnetic resonance perspective. *Prog. Nucl. Magn. Reson. Spectrosc.* **2023**, *134*, 20–38.
202. Tsuji, T.; Harada, S.; Teraji, T. Measuring the stress tensor in nitrogen-doped CVD diamond using solid-state quantum sensor. *Sci. Technol. Adv. Mater.* **2025**, *26*, 2546779.
203. Alam, M.S.; Gorrini, F.; Gawełczyk, M.; Wigger, D.; Coccia, G.; Guo, Y.; Shahbazi, S.; Bharadwaj, V.; Kubanek, A.; Ramponi, R. Determining strain components in a diamond waveguide from zero-field optically detected magnetic resonance spectra of negatively charged nitrogen-vacancy-center ensembles. *Phys. Rev. Appl.* **2024**, *22*, 024055.

204. Rodzoń, I.; Zhang, X.; Ivády, V.; Zheng, H.; Wickenbrock, A.; Budker, D. Temperature shift of magnetic field dependent photoluminescence features of nitrogen-vacancy ensembles in diamond. *Phys. Rev. B* **2025**, *111*, 094112.
205. Block, M.; Kobrin, B.; Jarmola, A.; Hsieh, S.; Zu, C.; Figueroa, N.; Acosta, V.M.; Minguzzi, J.; Maze, J.; Budker, D. Optically enhanced electric field sensing using nitrogen-vacancy ensembles. *Phys. Rev. Appl.* **2021**, *16*, 024024.
206. Mai, D.; Zhong, C.; Wang, Z.; Wang, H.; Sun, X.; Dai, R.; Wang, Z.; Zhang, Z. Megabar pressure sensing and magnetic phase imaging by [111]-oriented nitrogen-vacancy centers in diamond. *J. Appl. Phys.* **2025**, *138*, 045901.
207. Hilberer, A.; Toraille, L.; Dailledouze, C.; Adam, M.-P.; Hanlon, L.; Weck, G.; Schmidt, M.; Loubeyre, P.; Roch, J.-F. Enabling quantum sensing under extreme pressure: Nitrogen-vacancy magnetometry up to 130 GPa. *Phys. Rev. B* **2023**, *107*, L220102.
208. Shelton, D.P.; Cabriales, W.; Salamat, A. Magnetometry in a diamond anvil cell using nitrogen vacancy centers in a nanodiamond ensemble. *Rev. Sci. Instrum.* **2024**, *95*, 083901.
209. Dimarcq, N.; Gertsvolf, M.; Mileti, G.; Bize, S.; Oates, C.; Peik, E.; Calonico, D.; Ido, T.; Tavella, P.; Meynadier, F. Roadmap towards the redefinition of the second. *Metrologia* **2024**, *61*, 012001.

Disclaimer/Publisher's Note: The statements, opinions and data contained in all publications are solely those of the individual author(s) and contributor(s) and not of MDPI and/or the editor(s). MDPI and/or the editor(s) disclaim responsibility for any injury to people or property resulting from any ideas, methods, instructions or products referred to in the content.